

1  
2   **Was the October 9<sup>th</sup> 1995 M<sub>w</sub> 8 Jalisco, Mexico earthquake a near trench event?**  
3

4   **Vala Hjörleifsdóttir<sup>1</sup>, Hugo Samuél Sánchez Reyes<sup>2</sup>, Angel Ruiz Angulo<sup>3</sup>, Maria Teresa**  
5   **Ramírez-Herrera<sup>4</sup>, Rosío Castillo-Aja<sup>5</sup>, Shri Krishna Singh<sup>1</sup>, Chen Ji<sup>6</sup>**

6   <sup>1</sup>. Departamento de Sismología, Instituto de Geofísica, Universidad Nacional Autónoma de  
7   México, Ciudad de México,

8   <sup>2</sup>. Univ. Grenoble Alpes, CNRS, ISTerre, F-3800 Grenoble, France

9   <sup>3</sup>. Centro de Ciencias de la Atmósfera, Universidad Nacional Autónoma de México, Ciudad de  
10   México

11   <sup>4</sup>. Laboratorio Universitario de Geofísica Ambiental, IGG, Universidad Nacional Autónoma  
12   de México, Ciudad Universitaria, Ciudad de México

13   <sup>5</sup>. Posgrado en Geografía. Universidad Nacional Autónoma de México, Ciudad Universitaria,  
14   Ciudad de México.

15   <sup>6</sup>. Department of Earth Science, University of California, Santa Barbara, California

16   Corresponding author: Vala Hjörleifsdóttir (vala@igeofisica.unam.mx)

17

18   **Key Points:**

- 19   • The event nucleated at ~20 km depth and broke a >150 km long segment of the  
20   Mesoamerican Subduction Zone, rupturing towards the NW.  
21   • Two possible scenarios: 1) Slip between trench and coast as suggested by joint inversion  
22   of teleseismic records and nearfield static offsets.  
23   • 2) Coseismic slip near the trench and postseismic slip near coast, when allowing for  
24   effects of postseismic slip on the static offsets.

25

## 26 Abstract

27 The behavior of slip close to the trench during earthquakes is not well understood and  
28 observations of large earthquakes breaking the near trench fault surface are rare. The 1995  $M_w$   
29 8.0 Jalisco earthquake seems to have broken the near trench area, as evidenced by large  $M_s$ - $M_w$   
30 disparity, small high frequency radiated energy compared to total energy and low  $E_r/M_0$  ratios, in  
31 addition to several finite slip models showing large slip near the trench. However, slip models  
32 obtained using campaign GPS data, suggest slip near shore. In this study we try to answer  
33 whether this event was a near trench event or not, by inverting teleseismic P-, S-, Rayleigh and  
34 Love waves, as well as campaign GPS static offsets, either separately or jointly, to obtain the slip  
35 distribution on the fault as a function of time. We find two possible end member scenarios  
36 consistent with observed data: 1) coseismic slip distributed between coast and trench and no (or  
37 very little) postseismic slip and 2) coseismic slip principally near the trench with large (up to 1.8  
38 m) aseismic slip occurring in the first 5-10 days after the earthquake, with a total moment  
39 corresponding to 16% of that of the event. We are unable to distinguish between these two end  
40 member scenarios by tsunami modeling and finally are neither able to conclude or exclude that  
41 the event was a typical near trench event.

## 42 1 Introduction

43

44 The shallowest portion of the mega thrust interface in subduction zones has lower seismicity than  
45 the interface further downdip and has been thought to accommodate the relative plate motion by  
46 creep [Byrne *et al.*, 1988]. However, in some regions, this portion of the interface breaks in so  
47 called tsunami earthquakes [Kanamori, 1972; Lay *et al.*, 2012], such as the Sanriku 1896  
48 [Tanioka and Satake, 1996], Nicaragua 1992 [Kanamori and Kikuchi, 1993], Java 1994 [Polet  
49 and Thio, 2003] and Mentawai 2010 [Newman *et al.*, 2011; Hill *et al.*, 2012] earthquakes, or  
50 participates in large megathrust events, with exceptionally large slip, as in the 2011 Tohoku  
51 earthquake [Ito *et al.*, 2011; Sato *et al.*, 2011; Shao *et al.*, 2011; Simons *et al.*, 2011].

52

53 There are many unanswered questions about the relative behavior of the friction on the fault  
54 between this shallowest portion of the subduction zone interface and the further downdip  
55 segment typically considered seismogenic, for example, what controls the apparent downdip

56 segmentation? How does it vary between different subduction zones? Is the updip segment  
57 aseismically creeping in some zones? Can the updip portion break by itself, or do earthquakes  
58 have to nucleate and/or involve important slip in the downdip zone as well? The answers to  
59 these questions are important for the estimates of tsunami hazard as large slip in the updip zone  
60 produces a much larger tsunami than similar slip in the downdip zone. However, due to the long  
61 recurrence interval of large earthquakes and short time span of historical records, there are only a  
62 few regions where large earthquakes breaking the shallow parts of the interface have been  
63 observed.

64

65 Arguably, the clearest example of downdip segmentation is in the Japan Trench. Several  
66 earthquakes have broken the subduction interface during the last 150 years, notably by the 1896  
67 Sanriku earthquake that is considered to have broken only the shallow part of the interface  
68 [Tanioka and Satake, 1996], the 1978 and 2005 Miyagi-Oki earthquakes, that broke the further  
69 downdip segment [Seno *et al.*, 1980; Yamanaka and Kikuchi, 2004; Okada *et al.*, 2005], and the  
70 2011 Tohoku earthquake, which broke both the shallow and the deep parts of the subduction  
71 interface [Ammon *et al.*, 2011; Simons *et al.*, 2011] with an extraordinarily large slip of up to 60  
72 m [Ito *et al.*, 2011; Sato *et al.*, 2011; Shao *et al.*, 2011] on the shallow part. In this region, the  
73 near trench area has also been observed to slip in episodic slow-slip events [Ito *et al.*, 2015].  
74 Not only can the updip portion of the fault accommodate relative motion across it by creep or  
75 episodic slow slip, but so can the downdip portion, as well as some areas in the traditionally  
76 seismogenic zone (see for example Lay *et al.* [2012]). The interpretation is that the friction on  
77 the fault interface varies from place to place [Pacheco *et al.*, 1993].

78

79 In Mexico, the two largest subduction interface events recorded in the last 100 years, those of  
80 June 3<sup>rd</sup>, 1932, M<sub>S</sub> 8.2 [Abe, 1981] and October 9<sup>th</sup>, 1995, M<sub>w</sub> 8.0 [GlobalCMT], broke the same  
81 lateral segment of the Mesoamerican Trench (Fig. 1). Additionally, another large earthquake, the  
82 June 18<sup>th</sup>, 1932, M<sub>S</sub> 7.8 [Abe, 1981] event, broke the same segment. Several observations suggest  
83 that the 1932 and 1995 events were very different [Pacheco *et al.*, 1997]. High intensities and  
84 similar M<sub>S</sub> (8.2) versus M<sub>w</sub> (8.0) values were reported for the 1932 event [Singh *et al.*, 1985;  
85 Anderson *et al.*, 1989], whereas low intensities and a large discrepancy between m<sub>b</sub>/M<sub>S</sub> (6.6/7.4,  
86 USGS) versus M<sub>w</sub> (8.0, GlobalCMT) for the 1995 event [Ortiz *et al.*, 1998, 2000]. These

87 differences suggest that perhaps the 1995 event broke the shallower segment of the fault  
88 interface, whereas the 1932 event the deeper.

89

90 There is conflicting evidence from seismic [Mendoza and Hartzell, 1999; Mendoza *et al.*, 2011;  
91 Ye *et al.*, 2016, USGS Finite fault source model] and geodetic data [Melbourne *et al.*, 1997;  
92 Hutton *et al.*, 2001] on the location of the large slip during the 1995 event; the slip distributions  
93 obtained from seismic data show much shallower slip than those obtained from GPS data. Both  
94 types of models have their uncertainties and resolution issues, but the question remains, can both  
95 datasets be predicted by the same model?

96

97 In this study we aim to reconcile the different locations of large slip areas obtained by inverting  
98 seismic and geodetic data for the Jalisco 1995 earthquake. To do so, we invert seismic and  
99 geodetic recordings separately, as well as jointly. We find two possible scenarios; 1) a joint  
100 model with fairly uniform and purely coseismic slip between coast and trench and 2) coseismic  
101 slip principally near the trench and aseismic slip (slow slip or afterslip) in the 6 months before or  
102 5-10 days after the event, downdip of the coseismic slip. The tsunami wave height expected for  
103 each of the models is calculated, and compared with tsunami observations in an attempt to set  
104 further constraints on the source model.

105

## 106 **2 Seismic source modeling; Data and Methods**

### 107       2.1 Teleseismic data

108

109 Several digital, teleseismic, broadband recordings of the 1995 Jalisco earthquake are available.  
110 In this study we used P- and S-waves registered at 27 and 17 stations, respectively, with a  
111 relatively good azimuthal distribution, given the lack of high-quality stations in the Pacific basin  
112 (Fig. 2). Furthermore, we use Rayleigh, and Love waves registered at 17 and 13 stations,  
113 respectively. The stations are located at angular distances of 32 to 89 degrees from the  
114 hypocenter.

115

116 The P- and S-wave arrival times are picked manually, to remove the effect of 3D structure along  
117 their trajectories on the travel time of the waves. Considerable care was taken in this step to  
118 assure that all stations were aligned on the same phase. We deconvolved the instrument  
119 responses from the original records, resulting in displacement seismograms, which we  
120 subsequently band-passed between 1-100 seconds for the body-wave records and 170-250  
121 seconds for the surface-wave seismograms.

## 122 2.2 Static Displacements

123

124 The 1995 Jalisco earthquake is one of the first large earthquakes for which coseismic  
125 displacements were measured by GPS instruments. A campaign survey that measured locations  
126 of 11 sites in the Jalisco-Colima area was carried out in March/April of 1995. The sites were  
127 reoccupied 5-10 days after the October 9<sup>th</sup> earthquake [Melbourne *et al.*, 1997], roughly 6  
128 months after the initial measurement. Coseismic displacement vectors were calculated by  
129 Melbourne *et al.* [1997] and Hutton *et al.* [2001]. Both studies included 5-10 days of  
130 postseismic displacement in their estimates of coseismic displacement, due to the time spent to  
131 reoccupy the stations, as well as the aforementioned 6 months of pre-seismic displacements. In  
132 this study we mostly use the displacement vectors estimated by the second group Hutton *et al.*,  
133 [2001] as they considered more precise orbits for the calculations, however, the differences are  
134 not large between the two sets of estimated displacement vectors, and we will show that our  
135 results are minimally affected by this choice.

## 136 2.3 Subsidence and strong motion records

137

138 The observed subsidence at a tide gauge in Manzanillo harbor and on pressure sensors slightly  
139 offshore Barra de Navidad show subsidence of  $11.8 \pm 1.3$  cm and  $40 \pm 2$  cm respectively [Ortiz *et*  
140 *al.*, 2000]. We note that these observations were not used in previous geodetic studies and the  
141 subsidence estimate from the tide gauge corresponds to deformation during a different time  
142 window than the GPS data, making a direct comparison difficult. For these reasons we have not  
143 included the data points in the inverse modeling, but rather forward predicted the subsidence  
144 values at the Barra de Navidad site, to compare with our models for reference. The Manzanillo  
145 harbor site is very close to the CRIP GPS site.

146

147 Records from five accelerographic stations are available for this earthquake. Unfortunately,  
148 none of the stations are located within a fault length of the earthquake, and they were located on  
149 or near dams, with near-station effects heavily influencing the movements. Therefore we do not  
150 use these stations for the modeling.

151

## 152 2.5 Inversion Method

153

154 We invert the observed motions for the distribution of slip on the fault plane during the  
155 earthquake. The inversion is performed using the Fast Finite Fault (FFF) inversion algorithm [Ji  
156 *et al.*, 2002a, 2002b]. The algorithm uses a simulated annealing method, which minimizes the  
157 weighted difference between wavelet coefficients of observed and simulated seismograms. The  
158 slip on each subfault has an asymmetric time function [Ji *et al.*, 2003] and smoothing is applied  
159 both to the slip distribution and to the rupture contours [Shao *et al.*, 2011]. Static offsets cannot  
160 be modeled by wavelets and are included in the misfit function by a simple difference between  
161 observed and modeled displacements.

162

163 Several subjective choices of input parameters are necessary for the modeling. First, the size and  
164 orientation of the fault plane have to be fixed. The strike is relatively well determined by the  
165 orientation of the subduction zone, but an error in the dip angle can have an important effect on  
166 the solution. We use the dip of 13 degrees in this study, as an intermediate between the dip of  
167 the GlobalCMT solution (9°) and the dip of the slab model Slab1.0 which is 10-20° in this  
168 region, [Hayes *et al.*, 2012]. The rake is allowed to vary within ±45 degrees from an average  
169 rake of 90 degrees. The weights put on the misfit of scalar moment and the solution roughness  
170 are also important. However, amplitudes of surface waves are very sensitive to the scalar  
171 moment and when included in the inversion the weight on the scalar moment becomes  
172 unimportant. For reference we compare to the moment of the GlobalCMT solution,  
173  $M_0_{\text{ref}} = 1.15 \times 10^{21} \text{Nm}$ .

174

175 The slip on the fault plane is determined relative to the hypocenter. Therefore, the location of the  
176 hypocenter used has an effect on the geographical locations of the slip patches. Furthermore, the

177 depth can have an effect on the observed pattern of slip. In Mexico it has been noticed that  
178 hypocenters estimated from global data tend to be mislocated towards the northeast by on the  
179 order of 20 km [Singh and Lermo, 1985; Hjörleifsdóttir *et al.*, 2016], and we therefore use the  
180 hypocentral location reported by a local network (Red Sísmica del Estado de Colima, RESCO)  
181 (Lat. 18.81°N, Lon. 104.54°W, depth 17.0 km), however, we set the hypocenter depth to 20 km  
182 so that the fault plane does not reach the surface far from the trench.

183

184 Other subjective choices are the weight on each wavelet coefficient (the relative importance of  
185 different periods) and the relative weight of static, long period and body-wave data. Here we use  
186 the wavelet coefficients typically used in the FFF algorithm [Ji *et al.*, 2002a, 2002b]. We use  
187 the same weight on body and surface waves, but vary the relative importance of the static data.  
188 Furthermore, the reference rupture velocity has an important impact on the slip distribution. We  
189 will invert the data assuming both nearly fixed and variable rupture velocities.

190

### 191 **3 Seismic source modeling; Results**

#### 192       3.1 Teleseismic body and surface-wave inversion

193

194 First, we perform an inversion of body and surface waves together. The seismograms used are  
195 chosen based on station noise level, as well as to obtain a satisfactory azimuthal coverage. We  
196 then assign the strike of the fault plane to best match the orientation of the trench, and based on  
197 initial test inversions, we select a fault plane sufficiently large as to contain all the slip in the  
198 earthquake. In this set of inversions, we do not constrain the moment, as it is well constrained by  
199 the surface-waves. We use the Crust2.0 [Bassin *et al.*, 2000] velocity structure to describe the  
200 local structure at the source.

201

202 We inverted the observed seismograms for the slip distribution, assuming different values of  
203 nearly fixed rupture speeds  $v_r=1.5, 2.0, 2.5, 3.0$  km/s, allowing the speed to vary locally from the  
204 average value by  $\pm 0.1$  km/s (Fig. 3 a-d). Then we performed two more inversions, with average  
205 values of  $v_r=2.0, 2.5$  km/s, respectively, but permitting larger variations in the rupture speed of  
206  $\pm 0.8$  km/s (Fig. 3 e and f). All the resulting slip models have several things in common. They

207 all rupture two patches that are more or less connected, one near the hypocenter and one to the  
208 NW, reaching up to the trench. For small values of the rupture speed, the second patch is closer  
209 to the hypocenter than for higher values of the rupture speed. Larger slip is observed over a  
210 smaller area for smaller rupture speeds and vice versa. The comparison of observed and  
211 modeled seismograms for our best fitting model ( $v_r=var2.5$ , Fig. 3f) is shown in Fig. 4.

212

213 The predicted static displacements for all models are close to or larger than the observed in the  
214 SE, near CRIP, but only about half the observed near CHAM in the NW. We note that the  
215 higher rupture velocities,  $v_r=2.0$  or  $2.5$  km/s, generate better matches to the static data, which  
216 was not used in the modeling.

217

218 We find that the misfit to the various datasets and constraints decreases with increasing rupture  
219 speed. This observation should be taken with caution, as increasing the rupture speed effectively  
220 allows for a larger fault plane, or more free parameters. However, visibly poor fits for rupture  
221 velocity of 1.5 km/s indicates that an average rupture speed of 2 km/s or larger is required  
222 (waveforms and discussion are presented in supplementary material section S1, Figs. S1-S6).  
223 Furthermore, we find that the synthetic surface waves show a larger directivity effect than  
224 observed for  $v_r=3.0$  km/s. Allowing a variable rupture speed increases the number of free  
225 parameters further, so predictably the misfit is lower in the inversions with a larger range of  
226 allowed rupture speeds. However, we note that the slip distribution is very similar to the fixed  
227 rupture velocity model. Based on the mismatch between observed and predicted seismograms  
228 for rupture speeds of 1.5 km/s and 3.0 km/s, we estimate an average rupture speed of 2.0-2.5  
229 km/s.

230

231 However, the most notable result from these experiments is that all the models show that most of  
232 the slip occurs near the trench, with the amount of slip and size of fault patches varying only  
233 slightly with rupture speed. We performed various tests, varying the dip and the relative  
234 importance of the waveform misfit and the smoothness constraint in the inversion, and by large  
235 they show the same pattern.

236

237        3.2 Static Inversion  
238

239        We invert the 11 static displacement vectors estimated by *Hutton et al.* [2001] and *Melbourne et*  
240        *al.* [1997] (Fig. 5), using our preferred fault geometry. We find that there is little difference  
241        between the two. For each data set, we perform two inversions; 1) weight on each measurement  
242        is based on its error ( $w=1/\sigma$ , where  $\sigma$  is the displacement uncertainty reported in each of the  
243        studies) and 2) same weight on all measurements.

244

245        The results from these inversions agree in several characteristics with the slip distributions  
246        presented by *Melbourne et al.* [1997] and *Hutton et al.* [2001]. We observe most of the slip  
247        northwest from the hypocenter. We also found that the rupture is described by more than one  
248        slip patch even though we constrained the solution to be smooth. The large offsets measured at  
249        the nearest stations (CHAM, CRIP and PURI) have the largest effect on the static solutions, as  
250        previously pointed out by *Melbourne et al.* [1997]. The maximum slip obtained in our inversion  
251        is somewhat smaller than the results from *Melbourne et al.* [1997] and *Hutton et al.* [2001], who  
252        suggest a maximum slip of 4-5 m. However, we found that the location of the maximum slip  
253        along strike and dip are quite similar to those previously presented.

254

255        The majority of slip is located deeper and closer to the coast in this model than in the seismic  
256        models presented in the previous section. This is consistent with results of the previous studies,  
257        which suggest that the depth of the patch may reflect the incapacity of this network to resolve  
258        slip near the trench. We performed various tests to evaluate whether the depth of the slip was an  
259        artifact of the model parameters, and how it could be reconciled with the seismic models. We  
260        tried various dips of the faults plane, different weighting of the GPS vectors relative to each  
261        other, and weighting the horizontal components more strongly relative to the vertical component.  
262        However, all of the resulting models had the majority of slip much deeper than the seismic  
263        models.

264

265        We notice an unexpected trend in the change in the vertical component as a function of distance  
266        from the trench; from PURI to AYUT and GUAC. The typical pattern would be diminishing  
267        vertical motions with distance from the end of the slip model, however, out of these three

268 stations, we find the largest subsidence at AYUT, more than 150 km from the trench, indicating  
269 that perhaps the data at this station is erroneous. However, removing this station from the  
270 inversions does not show any significant changes in the slip pattern.

271  
272 The static model predicts large uplift offshore Barra de Navidad (BaNa), contrasting with the  
273 large subsidence observed there by a moored pressure sensor. The modeled uplift/subsidence is  
274 controlled by the spatial gradient of slip below the station, or in this case the mooring. As the  
275 model predicts artificial large slip at the bottom of the fault, due to anomalously large subsidence  
276 at AYUT, the spatial gradient is small close to BaNa and large uplift is predicted. By including  
277 this site in the inversion, it is relatively easy to produce large subsidence there, simply by  
278 concentrating the slip contours near it. However, we chose not to include this station in the  
279 inversion for two main reasons; 1) It does not cover the same time period as the GPS data, 2)  
280 strong currents due to the tsunami may have moved the mooring, in a similar way as they moved  
281 large sunken ships in the nearby lagoon [Filonov *et al.*, 1997].

282

### 283 3.3 Joint Inversion

284  
285 Finally we invert the body waves, surface waves and static displacements together, combining  
286 the datasets of the previous two sections. In these inversions we do not constrain the moment  
287 and we apply the same smoothing as for the seismic inversions. As one might guess from  
288 looking at the relatively different solutions in Fig. 3 and Fig. 5, both data sets are not very well  
289 matched by either of the single-dataset slip models. We perform several inversions, with  
290 increasing relative weights on the GPS-data set (Fig. 6) compared to the seismic data. Note that  
291 the absolute weight is not meaningful, however, as we increase it from 0.001 to 1.0 the effect  
292 goes from barely considering the GPS data to requiring it to be almost exactly matched.

293

294 We find that when the weight is small on the GPS data set, the slip distributions are very similar  
295 to the seismic only models, and that the GPS vectors at the eastern section of the fault (CRIP) are  
296 well fit, whereas the displacement vector at CHAM is relatively poorly fit, especially the vertical  
297 component. Increasing the weight on the GPS dataset predictably improves the match between  
298 observed and predicted static offset vectors, whereas the match to the seismic data deteriorates

somewhat, when the weight rises above 0.1 (waveforms for weight of 0.1 are shown in Fig. 7). Decreasing fit to the seismograms with increasing weight on the GPS data is not so easily observed by eye in the waveforms, however the overall scalar moment increases (from  $M_0/M_{0\_ref} = 1.08$  for weight 0.001 on GPS to  $M_0/M_{0\_ref} = 1.28$  for weight 1.0 on GPS), resulting in the surface waves being on average a bit too large (Supplement, section S2 and Fig S7-S12). We also see a slightly increased misfit to the first 20 seconds of the records at stations towards the north and northeast (for example stations FFC and LID) for a weight on GPS of 1.0. The slip models with large weight of the seismic data have large slip close to the trench, whereas the slip models with large weight on the static data have large slip near the coast, consistent with the results of previous sections. Intermediate results show relatively uniform slip between the coast and the trench.

310

Based on this analysis, we find that the models with weights on the static data of 0.1 or below provide predictions that can match the seismic data reasonably well, whereas weights on GPS data of 0.05 or higher give good matches to the static offsets (Fig. 6). We note that there is therefore a range of models that give reasonably good matches to both data sets simultaneously.

### 315 3.4 Comparison with previous slip models

316

Several studies have presented kinematic seismic source models of the 1995, Jalisco earthquake. Some characteristics of this earthquake appear in all the models; the rupture propagated to the north west of the hypocenter and the approximate length of the rupture was between 150 and 200 km. However, there is an important disagreement in the slip distributions obtained from the different types of data used in the analysis. Inversions for the rupture history based on inversion of broadband recordings of teleseismic body waves [Mendoza and Hartzell, 1999; Mendoza et al., 2011; Ye et al., 2016] as well as joint inversion of body and surface waves [USGS *finite fault solution*] show slip near the hypocenter followed by shallow slip, with maximum values of 3-4 m at a distance between 70 and 130 km NW of the hypocenter and at distances of 10-40 km from the trench. In contrast, the models presented by Melbourne et al. [1997] and Hutton et al. [2001] from the inversion of the available geodetic data, maximum slip values of 4-5 m were located at 55 km away from the trench in the downdip direction.

329

330 The slip models obtained when matching static and seismic data in this study are very similar to  
331 those obtained by other researchers using the corresponding data sets; the seismic slip model is  
332 similar to those presented by *Mendoza and Hartzell*, [1999], *Mendoza et al.*, [2011] and *Ye et al.*,  
333 [2016] and the USGS Finite fault slip model, whereas the static slip model resembles the models  
334 by *Melbourne et al.* [1997] and *Hutton et al.* [2001] obtained using the same dataset (Fig. 8). On  
335 one hand these results are reassuring, as using the same data leads to similar models, regardless  
336 of the details of the methods used. On the other hand the differences between the static and  
337 seismic models are disconcerting, as there can only be one true coseismic slip model.  
338

## 339 4 Discussion

### 340 4.1 Alternative model: Afterslip

341  
342 There are several indications that the 1995 Jalisco event produced small high-frequency radiation  
343 compared to other earthquakes; 1) ratios of total radiation to high-frequency radiation in Mexico  
344 City (at about 500 km distance) are high compared to other Mexican earthquakes and similar to  
345 ratios of events that are located near the trench [*Shapiro et al.*, 1998], 2) estimated energy-to-  
346 moment ratio,  $E_S/M_0 = 4.2\text{e-}6$ , is smaller than the ratios for other subduction zone events nearby  
347 [*Pérez- Campos and Beroza*, 2001; *Pérez-Campos et al.*, 2003], and similar to that of tsunami  
348 earthquakes [*Ye et al.*, 2016], 3) moreover, the October 9<sup>th</sup>, 1995 earthquake exhibited the largest  
349 disparity along the Mexican Subduction Zone between the estimated  $M_S$  (7.4) and the  $M_w$  (8.0)  
350 [*Pacheco et al.*, 1997].

351  
352 The small high frequency radiation by this event has grouped it together with tsunami or near  
353 trench earthquakes. However, the joint model, presented in the previous section, breaks (at least  
354 almost) all the way to the coast, making this event only partially a “near-trench” event.  
355

356 We will now show that there is an alternative model. Perhaps one of the most critical  
357 assumptions we have made up to this point is that the measured static displacement vectors  
358 include only the coseismic displacements and that no other slip occurred during the rest of the  
359 measurement period. However, rapid afterslip following this earthquake has been suggested,

360 based on the daily averages of the tidal record in Manzanillo (a few kilometers northeast of GPS  
361 station CRIP), compared to tidal records in Acapulco and Puerto Vallarta. This comparison  
362 shows a coseismic subsidence of 14 cm in Manzanillo, contrasting with  $7\pm2$  cm of uplift in the  
363 following four days [Melbourne *et al.*, 2002]. Given that the static offsets used in this study  
364 were measured 5-10 days after the event, this type of large early afterslip could significantly  
365 influence them.

366

367 We therefore hypothesize that there was a significant contribution to the measured geodetic  
368 offsets from aseismic slip, and further assume that the coseismic slip is well described by the  
369 seismic only models. As the tide gauge records suggest large afterslip, we will assume that the  
370 aseismic slip occurs after the event, although we cannot exclude that a significant part of it  
371 occurs in a slow-slip event in the 6 months before the earthquake. Furthermore, we do not  
372 consider the possibility of viscoelastic rebound causing postseismic motion, due to the short  
373 timescales involved. We can then pose the question of how much afterslip is required to match  
374 the difference between the predicted offsets for the seismic only model and the observed static  
375 offsets.

376

377 Next we assume that the difference in the seismic and geodetic models is due to afterslip. We  
378 can then estimate the static deformation due to the aseismic slip by subtracting the contribution  
379 of the coseismic slip, as predicted by our best coseismic model, from the observed static  
380 displacements. We use the coseismic slip model with a variable rupture velocity, centered on 2.5  
381 km/s (Fig. 3f). We now invert for the slip distribution of the aseismic event that best predicts the  
382 residual static deformation (Fig. 9a). We find highly localized slip of up to 1.8 meters offshore  
383 station CHAM, with slip above 1 meter in an elliptical area of about 40x60 km. Comparing the  
384 slip in the aseismic event to that during the seismic event (Fig. 9b), we see that the aseismic slip  
385 has little overlap with the coseismic slip and is nestled in the corner downdip of the shallower  
386 asperity and northwest of the deeper asperity of the coseismic slip distribution. It should be  
387 emphasized that the details of the slip distribution of the aseismic slip depends heavily on the  
388 coseismic slip model chosen for the modeling. However, all of the seismic only models show a  
389 large underestimate of the static offset of GPS station CHAM, indicating that most of the  
390 aseismic slip would have to occur near that station.

391

392 Interestingly, the seismic only models predict larger subsidence at CRIP (13.3 cm) than observed  
393 by the GPS station 6 days after the earthquake (6.2 cm; [Hutton *et al.*, 2001]; Fig. 3f), leading to  
394 a positive residual (7.1 cm), which requires uplift in the postseismic period. These predictions  
395 are consistent with observed tide gauge records [Melbourne *et al.*, 2002], which suggest  $14.2 \pm 2$   
396 cm subsidence during the earthquake and a gradual uplift of  $7 \pm 2$  cm during the following 6 days.  
397 We note that the close agreement between the subsidence and subsequent uplift predicted by our  
398 analysis and the tide gauge may be a coincidence, as both estimates have large errors. The  
399 subsidence values predicted by our modeling depend heavily on the choice of coseismic model  
400 and those estimated by the tide gauge measure the difference in sea level between two stations,  
401 which may depend on other factors than just the ground deformation, such as sea condition.  
402 However, we conclude that their overall agreement supports the general pattern of our model.

403

404 We find that the aftershocks located by a regional network [Pacheco *et al.*, 1997] are  
405 concentrated in the area between the maximums of the co-seismic and afterslip (Fig. 9b).  
406 Unfortunately, the timing information of these aftershocks has been lost. Locations of  
407 earthquake in this part of the Mesoamerican subduction zone by global networks are biased on  
408 average by 21 km towards  $62^\circ$  [Singh and Lermo, 1985; Hjörleifsdóttir *et al.*, 2016], but  
409 correcting for that bias, we can get an approximate location of the largest aftershocks from global  
410 networks (Fig 9b). Of the 35 aftershocks reported by NEIC during the first month after the  
411 earthquake, 7 of them occur within the first day after the earthquake and 23 within 5 days of the  
412 event. We do not see a time progression in the location of the aftershocks within this time  
413 period.

414

415 The afterslip inferred in this study is very rapid and large. The maximum afterslip ( $\sim 1.8$  m)  
416 within 5-10 days of the event is about half the maximum coseismic slip ( $\sim 3.5$  m). However, the  
417 scalar moment of the afterslip in the first 5-10 days is only 16% of the co-seismic moment.  
418 Similar rapid afterslip in the first day has been seen after other events; 20% of coseismic  
419 displacements in first day after the  $M_w$  6.3, 2009, L'Aquila, Italy, earthquake [Yano *et al.*,  
420 2014], 7% in the first 3 hours after the  $M_w$  7.6, 2012, Nicoya, Costa Rica, earthquake  
421 [Malservisi *et al.*, 2015], 30% in the first 24 hours after both the  $M_w$  7.6 1994 Sanriku-Haruka-

422 Oki, Japan, earthquake [Heki and Tamura, 1997] and the  $M_w$  7.8, 2010, Mentawai, Indonesia  
423 event [Hill *et al.*, 2012]. Furthermore, large afterslip to coseismic slip ratios have been observed  
424 for several other earthquakes in the Middle America Trench, such as the Pinotepa-  
425 Nacional/Ometepec  $M_w$  7.5 earthquake in 2012 [Graham *et al.*, 2014], the  $M_w$  7.2, 2012, El  
426 Salvador earthquake and the  $M_w$  6.9, 2004, October 9, Nicaragua earthquake [Geirsson *et al.*,  
427 2015].

428

429 It has been suggested that large afterslip relative to coseismic slip may be characteristic of  
430 tsunami type events, weakly coupled regions, as well as regions on the boundary between fault  
431 areas with velocity strengthening and weakening friction [Geirsson *et al.*, 2015]. This would  
432 suggests a transition from a more highly coupled region in the southeastern part of the fault plane  
433 slipping in the 1995 Jalisco event, to a fault patch with smaller coupling or conditionally stable  
434 creep in the northwestern part of the fault plane.

435

## 436 **4.2 Tsunami modeling**

437

438 In previous sections, we have obtained substantially different slip models that can predict  
439 observed seismic and/or static displacements. Some models show large slip near the trench, and  
440 others near the coast. These models could be expected to generate very different tsunamis. In  
441 order to test whether we can use the tsunami observations to distinguish between the different  
442 models, we carried out simulations for three representative slip models based on the joint  
443 inversions: a) adjusted to fit principally the seismic data (weight on GPS 0.001, Fig3a), b) joint  
444 model (weight on GPS 0.1, Fig3e) and c) adjusted to fit mostly the GPS data (weight on GPS 1,  
445 Fig3f). The tsunami numerical simulations were carried out with GeoClaw, a validated tsunami  
446 propagation model that solves the non-linear shallow water equations [LeVeque *et al.*, 2011]. A  
447 table of observed runup and details of the methodology used to calculate the tsunami wave  
448 height and propagation are presented in the supplementary material (Table S1, section S2,  
449 Synolakis, 1991; Borrero *et al.*, 1997; Geist, 1998, 2002; Jarvis *et al.*, 2008; Becker *et al.*, 2009;  
450 Černý *et al.*, 2016; Ramírez-Herrera *et al.*, 2016). Snapshots of the predicted wave height at 9  
451 minutes after the earthquake initiation time show that the crest of the seismic only model (model  
452 a) is higher, but has not arrived at the coast at this time. On the other hand, the joint (model b)

453 and static only model (model c), have wider crests, that have already arrived at the coast at this  
454 time (Figure 10a,b and c). Looking at other time frames, we find that the simulated arrival time  
455 for the first waves vary between 10-20 minutes, consistent with the reported times [Filonov,  
456 1997]. We also note that in the region between Chola, Jalisco to Caleta de Campos, Michoacán  
457 (between 75 and 100 km along the trench), the seismic model predicts larger wave heights than  
458 the static model, whereas the joint inversion predicts an intermediate value. All three models  
459 show peaks of local amplification at two locations along the coast that are not related to the  
460 arrival of the first wave, with the maximum amplitude occurring more than 40 minutes after the  
461 first arrival.

462

463 A similar observation can be made by comparing the modeled tsunami waveforms with pressure  
464 recorded by a CTD mooring deployed at 30 m depth offshore Barra de Navidad [Ortiz *et al.*,  
465 2000]. We find that the timing of the first arrivals for the seismic only and joint models (models  
466 a and b) are later than observed, whereas the first arrival for the static only model (model c) are  
467 slightly earlier. The amplitude of the waveforms cannot be directly compared, as the pressure  
468 sensor is not moored at the bottom but at 20 m above the seafloor which induces pendular  
469 movements as the mooring moves horizontally and down with the tsunami waves, inducing  
470 additional pressure. We have scaled the observed waveform by 0.5 for comparison. The  
471 maximum difference in the arrival time of the first tsunami wave between models is on the order  
472 of 5 minutes.

473

474 We find that only few of the runup observations show a fair agreement with the tsunami  
475 simulations (Fig. 10 e). In particular, the middle section of the domain does not have a good  
476 agreement between observed and simulation. This is consistent with recent work by Mori *et al.*,  
477 [2017], who model the tsunami produced by a seismic only slip model for this event, and find  
478 that the predicted tsunami is much smaller than observed. The morphology of the Manzanillo  
479 area is relatively complex as it has several bays that are known to be prone to resonance effects  
480 (see for example Okal and Synolakis, [2015]). The largest observed runup occurs in one of the  
481 bays of the Manzanillo region, consistent with our simulations. Furthermore, most of the  
482 measurements are made in bays, where the waves can amplify, possibly biasing the observations  
483 to larger values. Unfortunately, the resolution of the available bathymetry data limits the

484 possibility of proper simulations including runup and inundation areas. This could be resolved  
485 by future work that includes higher resolution bathymetry and topography, allowing for more  
486 accurate simulations. We therefore conclude that we are not able to use the tsunami modeling to  
487 distinguish between the end member scenarios.

488       4.3 Relatively high average rupture speed

489

490 Typically, earthquakes that break the near trench area have slow rupture speeds, which can be as  
491 low as 1.0 km/s [Kanamori and Kikuchi, 1993; Ammon *et al.*, 2006]. On the contrary, the 1995  
492 event had an average rupture speed of 2-2.5 km/s, which is typical for subduction zone  
493 earthquakes at traditionally seismogenic depths. This is a relatively robust result, as models with  
494 average rupture speeds of as high as 1.5 km/s generate substantially poorer fits to the observed  
495 seismograms than the more rapid ones. This may be explained in at least two ways; 1) the  
496 shallow fault plane properties in the Jalisco area are more similar to those at greater depth than in  
497 other subduction zones, 2) the earthquake ruptured both the shallow and the deeper part, as  
498 suggested by the joint models that have similar relative weights on the seismic and static  
499 observations (Fig. 6 (c) and (d)) and the average speed is a combination of a faster rupture at  
500 depth and a slower rupture near the trench. Analyzing the rupture contours for the inversions  
501 where variable rupture speed was allowed, we find that indeed the rupture speed in the shallow  
502 large-slip patches is as low as 1-1.5 km/s for both the seismic only and joint solutions (Fig. 11),  
503 consistent with the second explanation above. However, the variations in rupture speed along  
504 the fault plane are not well resolved and although this is finding is suggestive, it is not robust.  
505 Furthermore, we cannot resolve systematic variations in the rise time along the rupture plane.

506       4.4 Recurrence times

507

508 The Mw 8.0 1995 Jalisco event, together with the Mw 8.2 1932 Jalisco and Mw 8.0 1985  
509 Michoacán earthquakes, are the three largest events to break the Mexican subduction interface in  
510 the last 100 years. It is somewhat surprising that two of these events break the same segment of  
511 the subduction zone. When should we expect the next event in this segment? The answer to this  
512 question depends on whether there was significant overlap between the rupture areas in the two

513 events or not. Based on high seismic intensities, it has been suggested that the 1932 earthquake  
514 broke the fault surface near the coast [Singh *et al.*, 1985].

515  
516 Comparing the slip in the 1995 earthquake, of about 2 m over a large part of the rupture area  
517 (although reaching 3.5 m in the large slip patches), to the convergence rate between the Rivera  
518 and the North American plate, of about 3.3 cm/year [DeMets *et al.*, 2010] or increasing from  
519 3.9-4.8 cm/year going southeast along the rupture [Bandy, 1992; Kostoglodov and Bandy, 1995],  
520 and supposing that the plates are fully coupled, we would expect this type of event every 45-60  
521 years or so.

522  
523 The recurrence interval of the 1932 June 3<sup>rd</sup> event, supposing it had a coseismic slip of 3-5 m  
524 (somewhat larger than the 1995 event) and that there was little spatial overlap between that and  
525 the 1995 events may be on the order of 100-200 years. This recurrence interval suggests that we  
526 could expect another 1932 Jalisco earthquake in the next 100 years, with possibly severe  
527 consequences for this now much more populated area. However, the two end member scenarios  
528 have slip (either coseismic or seismic) close to the cost, suggesting a possible overlap between  
529 the 1932 and 1995 rupture. This would indicate that the some of the accumulated slip deficit was  
530 released in this event, which may delay the next event in this segment.

531

## 532 **5 Conclusions**

533  
534 We invert for the slip during the 1995 M<sub>w</sub> 8.0 Jalisco, Mexico, earthquake, using seismic and  
535 geodetic (campaign GPS) data. We find that the slip distribution depends heavily on the dataset  
536 used; slip in a deeper patch near the hypocenter and in a shallower patch towards the trench  
537 when using seismic data and slip in two patches close to the coast when using geodetic data.  
538 These results are very similar to those of other authors using the same datasets. Joint inversions  
539 of both datasets simultaneously show relatively uniform slip between the coast and the trench.  
540 The 1995 earthquake has macroseismic properties, such as the ratio between radiated energy to  
541 moment, typical for tsunami or near trench earthquakes. However, although the joint inversion  
542 shows larger slip close to the trench than typical for Mexican earthquakes, there is substantial

543 slip deep into the zone typically considered seismogenic. This is atypical for earthquakes with  
544 macroseismic properties similar to those of tsunami earthquakes.

545

546 Alternatively, we obtain a different model by allowing for rapid postseismic slip affecting the  
547 observed static offsets. With this assumption we find that more than 1 m of aseismic slip occurs  
548 in an elliptical area of about 40x60 km, most likely as afterslip during the 5-10 days after the  
549 earthquake. The afterslip fits into a “gap” in the coseismic slip model, downdip of the shallower  
550 slip patch, and to the northwest of the deeper slip patch. Most of the aftershocks occur on the  
551 boundary between the coseismic and aseismic slip areas. Slow-slip events have been observed in  
552 the same region as the afterslip reported in this study. The aseismic slip could significantly  
553 increase the expected recurrence interval of earthquakes in this zone.

554

555 We model the tsunami resulting from three representative models, but we were not able to  
556 discriminate between them based on the comparison of observed and modeled tsunami wave  
557 height. We find that the average rupture speed (2-2.5 km/s) is more similar to that of typical  
558 subduction earthquakes than the tsunami earthquakes that often break the near trench area,  
559 although this average may be a combination of a faster rupture at depth and a slower shallower  
560 rupture speed.

561

562 The assumptions that there is no postseismic motion (joint inversion) or that all the difference  
563 between seismic and geodetic models are due to postseismic motions can be seen as two  
564 permissible end member models. It is plausible that the true model is somewhere in between  
565 these two scenarios, and that the Jalisco earthquake was only partially a “near trench”  
566 earthquake.

## 567 Acknowledgments and Data

568 We thank Ryota Hino for helpful discussions. All data used in this paper has either been  
569 previously published or is publically available. Seismograms were obtained from the open  
570 access database of the Incorporated Research Institutions for Seismology (IRIS), networks II, IU  
571 and G, and geodetic and tsunami data from published literature as explained in text. Graphics  
572 were prepared using the Generic Mapping Tools (GMT, Wessel and Smith). Hjörleifsdóttir

573 thanks UNAM/DGAPA/PAPIIT grants: IB101812, IN111316, Ramírez-Herrera thanks PASPA-  
574 DGAPA-2015 and SEP-CONACYT grant No. 129456. Castillo-Aja thanks for CONACYT  
575 Ph.D. scholarship. Slip models can be accessed on the finite-source rupture model database  
576 (SRCMOD).

577

578

## References

- 579 Abe, K. (1981), Magnitudes of large shallow earthquakes from 1904 to 1980, *Phys Earth Planet  
580 In*, 27(1), 72–92, doi:10.1016/0031-9201(81)90088-1.
- 581 Ammon, C., T. Lay, H. Kanamori, and M. Cleveland (2011), A rupture model of the 2011 off the  
582 Pacific coast of Tohoku Earthquake, *Earth, Planets and Space*, 63(7), 33,  
583 doi:10.5047/eps.2011.05.015.
- 584 Ammon, C. J., H. Kanamori, T. Lay, and A. A. Velasco (2006), The 17 July 2006 Java tsunami  
585 earthquake, *Geophysical Research Letters*, 33, L24308, doi:10.1029/2006GL028005.
- 586 Anderson, J., S. Singh, Espindola, and Yamamoto (1989), Seismic strain release in the Mexican  
587 subduction thrust, *Physics of the Earth and Planetary Interiors*, 58(4), 307322,  
588 doi:10.1016/0031-9201(89)90102-7.
- 589 Bandy, W. (1992), Geological and geophysical investigation of the Rivera-Cocos plate  
590 boundary: Implications for plate fragmentation, Universidad Nacional Autonoma de Mexico.
- 591 Bassin, C., G. Laske, and G. Masters (2000), The Current Limits of Resolution for Surface Wave  
592 Tomography in North America, EOS Trans. AGU, Fall Meeting Suppl., vol. 81(48), p. F897.
- 593 Becker, Sandwell, W. Smith, Braud, Binder, J. Depner, Fabre, Factor, Ingalls, and Kim (2009),  
594 Global bathymetry and elevation data at 30 arc seconds resolution: SRTM30\_PLUS, *Marine  
595 Geodesy*, 32(4), 355–371, doi:10.1080/01490410903297766.
- 596 Bird, P. (2003), An updated digital model of plate boundaries, *Geochemistry, Geophysics,  
597 Geosystems*, 4(3), doi:10.1029/2001GC000252.
- 598 Borrero, J., M. Ortiz, V. Titov, and C. Synolakis (1997), Field survey of Mexican tsunami  
599 produces new data, unusual photos, *Eos, Transactions American Geophysical Union*, 78(8), 85–  
600 88, doi:10.1029/97EO00054.

- 601 Byrne, D., D. Davis, and L. Sykes (1988), Loci and maximum size of thrust earthquakes and the  
602 mechanics of the shallow region of subduction zones, *Tectonics*, 7(4), 833–857,  
603 doi:10.1029/TC007i004p00833.
- 604 Carrillo-Martinez, M. (1997), Isosistas Locales del Sismo de Manzanillo del 9 de Octubre de  
605 1995, 9:36 a.m., Estados de Colima y Jalisco, Mexico, *Revista Mexicana de Ciencias*  
606 *Geologicas*, 14(1), 110–113.
- 607 Černý, J., M.-T. Ramírez-Herrera, M.-F. Bógalo, A. Goguitchaichvili, R. Castillo-Aja, J.  
608 Morales, J. Sanchez-Cabeza, and A. Ruiz-Fernández (2016), Magnetic record of extreme marine  
609 inundation events at Las Salinas site, Jalisco, Mexican Pacific coast, *International Geology*  
610 *Review*, 58(3), 342–357, doi:10.1080/00206814.2015.1075230.
- 611 DeMets, C., R. Gordon, and D. Argus (2010), Geologically current plate motions, *Geophys J Int*,  
612 181(1), 1–80, doi:10.1111/j.1365-246x.2009.04491.x.
- 613 Filonov, A. (1997), Researchers study tsunami generated by Mexican earthquake, *EOS*, 78(3),  
614 21–25, doi:10.1029/97EO00014.
- 615 Geirsson, H., P. LaFemina, C. DeMets, D. Hernandez, G. Mattioli, R. Rogers, M. Rodriguez, G.  
616 Marroquin, and V. Tenorio (2015), The 2012 August 27 Mw 7.3 El Salvador earthquake:  
617 expression of weak coupling on the Middle America subduction zone, *Geophysical Journal*  
618 *International*, 202(3), 1677–1689, doi:10.1093/gji/ggv244.
- 619 Geist, E. (1998), Local tsunamis and earthquake source parameters, *Advances in Geophysics*, 39,  
620 117–209.
- 621 Geist, E. (2002), Complex earthquake rupture and local tsunamis, *Journal of Geophysical*  
622 *Research: Solid Earth (1978–2012)*, 107(B5), ESE 2–1–ESE 2–15, doi:10.1029/2000JB000139.
- 623 Graham, DeMets, Cabral-Cano, Kostoglodov, Walpersdorf, Cotte, Brudzinski, McCaffrey, and  
624 Salazar-Tlaczani (2014), GPS constraints on the 2011–2012 Oaxaca slow slip event that preceded  
625 the 2012 March 20 Ometepec earthquake, southern Mexico, *Geophysical Journal International*,  
626 197(3), 1593–1607, doi:10.1093/gji/ggu019.
- 627 Hayes, G. P., D. J. Wald, and R. L. Johnson (2012), Slab1.0: A three-dimensional model of  
628 global subduction zone geometries, *Journal of Geophysical Research: Solid Earth*, 117(B1),  
629 doi:10.1029/2011JB008524.
- 630 Hill, E. M. et al. (2012), The 2010 Mw 7.8 Mentawai earthquake: Very shallow source of a rare  
631 tsunami earthquake determined from tsunami field survey and near-field GPS data, *Journal of*

- 632 *Geophysical Research: Solid Earth*, 117(B6), doi:10.1029/2012JB009159.
- 633 Hjörleifsdóttir, V., S. Singh, and A. Husker (2016), Differences in Epicentral Location of  
634 Mexican Earthquakes between Local and Global Catalogs: An update, *Geofísica Internacional*,  
635 55(1), 79–93.
- 636 Hutton, W., C. DeMets, O. Sánchez, G. Suárez, and J. Stock (2001), Slip kinematics and  
637 dynamics during and after the 1995 October 9 Mw =8.0 Colima-Jalisco earthquake, Mexico,  
638 from GPS geodetic constraints, *Geophysical Journal International*, 146, doi:10.1046/j.1365-  
639 246X.2001.00472.x.
- 640 Ito, Y., T. Tsuji, Y. Osada, M. Kido, D. Inazu, Y. Hayashi, H. Tsushima, R. Hino, and H.  
641 Fujimoto (2011), Frontal wedge deformation near the source region of the 2011 Tohoku-Oki  
642 earthquake, *Geophysical Research Letters*, 38(7), doi:10.1029/2011gl048355.
- 643 Ito, Y., R. Hino, S. Suzuki, and Y. Kaneda (2015), Episodic tremor and slip near the Japan  
644 Trench prior to the 2011 Tohoku-Oki earthquake, *Geophys Res Lett*, 42(6), 1725–1731,  
645 doi:10.1002/2014gl062986.
- 646 Ji, C., D. Wald, and D. Helmberger (2002a), Source Description of the 1999 Hector Mine,  
647 California, Earthquake, Part I: Wavelet Domain Inversion Theory and Resolution Analysis, *B  
648 Seismol Soc Am*, 92(4), 1192–1207, doi:10.1785/0120000916.
- 649 Jarvis, A., H. I. Reuter, A. Nelson, and E. Guevara (2008), Hole-filled SRTM for the globe  
650 Version 4, available from the CGIAR-CSI SRTM 90m Database,
- 651 Ji, C., D. J. Wald, and D. V. Helmberger (2002b), Source Description of the 1999 Hector Mine,  
652 California, Earthquake, Part II: Complexity of Slip History, *Bulletin of the Seismological Society  
653 of America*, 92(4), 1208–1226, doi:10.1785/0120000917.
- 654 Ji, C., D. V. Helmberger, D. J. Wald, and K. Ma (2003), Slip history and dynamic implications  
655 of the 1999 Chi-Chi, Taiwan, earthquake, *Journal of Geophysical Research: Solid Earth*,  
656 108(B9), doi:10.1029/2002jb001764.
- 657 Kanamori, H. (1972), Mechanism of tsunami earthquakes, *Physics of the Earth and Planetary  
658 Interiors*, 6(5), 346–359, doi:10.1016/0031-9201(72)90058-1.
- 659 Kanamori, H., and M. Kikuchi (1993), The 1992 Nicaragua earthquake: a slow tsunami  
660 earthquake associated with subducted sediments, *Nature*, 361(6414), 714–716.
- 661 Kostoglodov, V., and W. Bandy (1995), Seismotectonic constraints on the convergence rate  
662 between the Rivera and North American plates, *Journal of Geophysical Research: Solid Earth*,

- 663 100(B9), 17977–17989, doi:10.1029/95JB01484.
- 664 Lander, J. F., L. S. Whiteside, and P. A. Lockridge (2003), Two Decades of Global Tsunamis  
665 1982–2002, *Science of Tsunami Hazards*, 21(1), 1–88.
- 666 Lay, T., H. Kanamori, C. J. Ammon, K. D. Koper, A. R. Hutko, L. Ye, H. Yue, and T. M.  
667 Rushing (2012), Depth-varying rupture properties of subduction zone megathrust faults, *Journal*  
668 *of Geophysical Research: Solid Earth*, 117(B4), doi:10.1029/2011JB009133.
- 669 LeVeque, R., D. George, and M. Berger (2011), Tsunami modelling with adaptively refined  
670 finite volume methods, *Acta Numerica*, 211–289, doi:10.1017/S0962492911000043.
- 671 Malservisi, R. et al. (2015), Multiscale postseismic behavior on a megathrust: The 2012 Nicoya  
672 earthquake, Costa Rica, *Geochemistry, Geophysics, Geosystems*, 16(6), 1848–1864,  
673 doi:10.1002/2015GC005794.
- 674 Melbourne, T., I. Carmichael, C. DeMets, K. Hudnut, O. Sanchez, J. Stock, G. Suarez, and F.  
675 Webb (1997), The geodetic signature of the M8.0 Oct. 9, 1995, Jalisco Subduction Earthquake,  
676 *Geophysical Research Letters*, 24(6), 715–718, doi:10.1029/97GL00370.
- 677 Melbourne, T. I., F. H. Webb, J. M. Stock, and C. Reigber (2002), Rapid postseismic transients  
678 in subduction zones from continuous GPS, *Journal of Geophysical Research: Solid Earth*,  
679 107(B10), ETG 10–1–ETG 10–10, doi:10.1029/2001JB000555.
- 680 Mendoza, C., and S. Hartzell (1999), Fault-slip distribution of the 1995 Colima-Jalisco, Mexico,  
681 earthquake, *Bulletin of the Seismological Society of America*, 89(5), 1338–1344,  
682 doi:10.1029/98GL02059.
- 683 Mendoza, C., Castro Torres, and Gomez Gonzalez (2011), Moment-Constrained Finite-Fault  
684 Analysis Using Teleseismic P Waves: Mexico Subduction Zone, *Bulletin of the Seismological*  
685 *Society of America*, 101(6), 2675–2684, doi:10.1785/0120100126.
- 686 Newman, A., G. Hayes, Y. Wei, and J. Convers (2011), The 25 October 2010 Mentawai tsunami  
687 earthquake, from real-time discriminants, finite-fault rupture, and tsunami excitation,  
688 *Geophysical Research Letters*, 38(5), doi:10.1029/2010GL046498.
- 689 Okada, T., T. Yaginuma, N. Umino, T. Kono, T. Matsuzawa, S. Kita, and A. Hasegawa (2005),  
690 The 2005 M7.2 MIYAGI-OKI earthquake, NE Japan: Possible rerupturing of one of asperities  
691 that caused the previous M7.4 earthquake, *Geophys Res Lett*, 32(24),  
692 doi:10.1029/2005GL024613.
- 693 Okal, E. A., and C. E. Synolakis (2015), Sequencing of tsunami waves: why the first wave is not

- 694 always the largest, *Geophysical Journal International*, 204(2), 719–735, doi:10.1093/gji/ggv457.
- 695 Ortiz, Kostoglodov, Singh, and Pacheco (2000), New constraints on the uplift of October 9, 1995
- 696 Jalisco-Colima earthquake (M, *Geofísica Internacional*, 39(4), 349–357.
- 697 Ortiz, M., S. Singh, J. Pacheco, and V. Kostoglodov (1998), Rupture length of the October 9,
- 698 1995 Colima- Jalisco Earthquake (Mw 8) estimated from tsunami data, *Geophysical Research*
- 699 *Letters*, 25(15), 2857–2860, doi:10.1029/98GL02059.
- 700 Pacheco et al. (1997), The October 9, 1995 Colima-Jalisco, Mexico Earthquake (Mw 8): An
- 701 aftershock study and a comparison of this earthquake with those of 1932, *Geophysical Research*
- 702 *Letters*, 24(17), 2223–2226, doi:10.1029/97GL02070.
- 703 Pacheco, J. F., L. R. Sykes, and C. H. Scholz (1993), Nature of seismic coupling along simple
- 704 plate boundaries of the subduction type, *Journal of Geophysical Research: Solid Earth* , 98(B8),
- 705 14133–14159, doi:10.1029/93JB00349.
- 706 Pérez-Campos, X., and G. C. Beroza (2001), An apparent mechanism dependence of radiated
- 707 seismic energy, *Journal of Geophysical Research: Solid Earth* , 106(B6), 11127–11136,
- 708 doi:10.1029/2000jb900455.
- 709 Pérez-Campos, X., S. Singh, and G. Beroza (2003), Reconciling Teleseismic and Regional
- 710 Estimates of Seismic Energy, *Bulletin of the Seismological Society of America*, 93(5), 2123–
- 711 2130, doi:10.1785/0120020212.
- 712 Polet, J., and H. Thio (2003), The 1994 Java tsunami earthquake and its “normal” aftershocks,
- 713 *Geophysical Research Letters*, 30(9), 1474, doi:10.1029/2002GL016806.
- 714 Ramírez-Herrera, M., M. Bógalo, J. Černý, A. Goguitchaichvili, N. Corona, M. Machain, A.
- 715 Edwards, and S. Sosa (2016), Historic and ancient tsunamis uncovered on the Jalisco-Colima
- 716 Pacific coast, the Mexican subduction zone, *Geomorphology*, 259, 90–104,
- 717 doi:10.1016/j.geomorph.2016.02.011.
- 718 Reyes, A., J. N. Brune, and C. Lomnitz (1979), Source mechanism and aftershock study of the
- 719 Colima, Mexico earthquake of January 30, 1973, *Bulletin of the Seismological Society of*
- 720 *America*, 69(6), 1819–1840.
- 721 Sato, M., T. Ishikawa, N. Ujihara, S. Yoshida, M. Fujita, M. Mochizuki, and A. Asada (2011),
- 722 Displacement Above the Hypocenter of the 2011 Tohoku-Oki Earthquake, *Science*, 332(6036),
- 723 1395–1395, doi:10.1126/science.1207401.
- 724 Seno, T., K. Shimazaki, P. Somerville, and K. Sudo (1980), Rupture process of the Miyagi-Oki,

- 725 Japan, earthquake of June 12, 1978, *Physics of the Earth and Planetary Interiors*, 23, 39–61.
- 726 Shao, G., X. Li, C. Ji, and T. Maeda (2011), Focal mechanism and slip history of the 2011 Mw  
727 9.1 off the Pacific coast of Tohoku Earthquake, constrained with teleseismic body and surface  
728 waves, *Earth Planets Space*, 63(7), 9, doi:10.5047/eps.2011.06.028.
- 729 Shapiro, N., S. Singh, and J. Pacheco (1998), A fast and simple diagnostic method for identifying  
730 tsunamigenic earthquakes, *Geophysical Research Letters*, 25(20), 3911–3914,  
731 doi:10.1029/1998GL900015.
- 732 Simons, M. et al. (2011), The 2011 magnitude 9.0 Tohoku-Oki earthquake: Mosaicking the  
733 megathrust from seconds to centuries, *Science*, 332, 1421–1425, doi:10.1126/science.1206731.
- 734 Singh, SK, and J Lermo (1985), Mislocation of Mexican earthquakes as reported in  
735 international bulletins, *Geofísica Internacional*, 24(2).
- 736 Singh, S., L. Ponce, and S. Nishenko (1985), The great Jalisco, Mexico, earthquakes of 1932:  
737 Subduction of the Rivera plate, *Bulletin of the Seismological Society of America*, 75(5), 1301–  
738 1313.
- 739 Singh, S., J. Pacheco, L. Alcántara, G. Reyes, M. Ordaz, A. Iglesias, Alcocer, C. Gutierrez, C.  
740 Valdés, and V. Kostoglodov (2003), A preliminary report on the Tecumán, Mexico earthquake  
741 of 22 January 2003 (Mw 7.4) and its effects, *Seismological Research Letters*, 74.
- 742 Synolakis, C. (1991), Tsunami runup on steep slopes: How good linear theory really is, *Natural  
743 Hazards*, 4, 221–234.
- 744 Tanioka, Y., and K. Satake (1996), Fault parameters of the 1896 Sanriku tsunami earthquake  
745 estimated from tsunami numerical modeling, *Geophysical Research Letters*, 23(13), 1549–1552,  
746 doi:10.1029/96GL01479.
- 747 UNAM Seismology Group (1986), The September 1985 Michoacán earthquakes: Aftershock  
748 distribution and history of rupture, *Geophysical Research Letter*, 13(6), 573–576,  
749 doi:10.1029/GL013i006p00573.
- 750 Yamanaka, Y., and M. Kikuchi (2004), Asperity map along the subduction zone in northeastern  
751 Japan inferred from regional seismic data, *Journal of Geophysical Research: Solid Earth*,  
752 109(B7), doi:10.1029/2003JB002683.
- 753 Yano, T. E., G. Shao, Q. Liu, C. Ji, and R. J. Archuleta (2014), Coseismic and potential early  
754 afterslip distribution of the 2009 Mw 6.3 L’Aquila, Italy earthquake, *Geophysical Journal  
755 International*, 199(1), 23–40, doi:10.1093/gji/ggu241.

756 Ye, L., T. Lay, H. Kanamori, and L. Rivera (2016), Rupture characteristics of major and great  
757 ( $M_w \geq 7.0$ ) megathrust earthquakes from 1990 to 2015: 1. Source parameter scaling  
758 relationships, *J Geophys Res Solid Earth*, 121(2), 826–844, doi:10.1002/2015jb012426.

759

760

761

762 **Figure Captions**

763

764 **Figure 1.** Tectonic context of the 1995 earthquake, as well as rupture areas of large earthquakes  
765 in the region (gray circles) [1973 - Reyes *et al.*, 1979; 1932, 2003 - Singh *et al.*, 1985, 2003;  
766 1985 - UNAM Seismology Group, 1986; 1995 - Pacheco *et al.*, 1997], localities referred to in  
767 text and plate boundaries [Bird, 2003].

768

769 **Figure 2.** Data used in this study; observed static displacements measured at GPS stations  
770 (aquamarine triangles), subsidence measured at pressure gauges (blue triangles), post tsunami  
771 field survey runup height estimates (peach bars), seismic stations (black triangles on inset).

772

773 **Figure 3.** Slip distributions obtained from seismic data (body and surface waves). Observed  
774 horizontal and vertical displacements (Hutton *et al.*, 2001) are shown with black and gray  
775 vectors, whereas horizontal and vertical displacements predicted by the slip model are shown  
776 with yellow and blue vectors. The slip distributions in panels a)-d) are obtained by fixing the  
777 rupture speed to values of 1.5, 2.0, 2.5 and 3.0 km/s. In the last two panels, the rupture speed was  
778 allowed to vary from a range of e) 1.2-2.8 and f) 1.7-3.2. We do not invert for the subsidence  
779 observed at the pressure sensor at Barra de Navidad (BaNa).

780

781 **Figure 4.** Observed (black) and synthetic (red) teleseismic a) body waves, b) surface waves for  
782 the model shown in Fig 3f. Labels on each station indicate from top to bottom, left to right,  
783 Vertical (P/UD) and transverse (SH) component, the station name, azimuth from the source,  
784 angular distance and relative amplitude of each trace.

785

786 **Figure 5.** Slip distributions obtained from geodetic data (static offsets obtained from repeat  
787 campaign GPS measurements). Observed horizontal and vertical displacements are shown with  
788 black and gray vectors, whereas horizontal and vertical displacements predicted by the slip  
789 model are shown with yellow and blue vectors. The slip distributions in panels a) and b) are  
790 obtained for displacements estimated by Hutton *et al.* (2001) and those in panels c) and d) from  
791 Melbourne *et al.* (1997). Panels a) and c) have weights on the individual stations that depend on  
792 the errors, whereas for panels b) and d) all stations have equal weights. We do not invert for the  
793 subsidence observed at the pressure sensor at Barra de Navidad (BaNa).

794

795 **Figure 6.** Slip distributions obtained from seismic (body and surface waves) together with  
796 geodetic data, displacement vectors same as in Fig. 3. The panels a to f have increasing weight  
797 on the GPS dataset relative to the seismic, as marked. We do not invert for the subsidence  
798 observed at the pressure sensor at Barra de Navidad (BaNa).

799

800 **Figure 7.** Teleseismic waveforms for joint seismic and geodetic slip model, with weight 0.1 (Fig  
801 6e). Labels same as Fig. 4.

802

803 **Figure 8.** Comparison of slip models obtained in this study (colors) to those obtained by other  
804 researchers (contours). a) Our seismic only model (variable rupture velocity,  $v_r = 1.9 - 3.1$ ),  
805 versus the seismic only model of Mendoza et al. (1999), contour lines every 0.5 m, b)  
806 Comparison of our geodetic only model, to the geodetic only model by Hutton et al. (2001),  
807 contour lines every 1 m.

808

809 **Figure 9.** Modeling the displacements not predicted by the seismic only model a) Black vectors  
810 show residual between the observed displacements (Hutton et al., 2001) and those predicted by  
811 our preferred seismic only model (variable rupture velocity,  $v_r = 1.9 - 3.1$ ). The slip model shown  
812 is that which best predicts the differences, and the colored vectors are the displacements  
813 predicted by this model. b) Our preferred seismic model shown with colors, overlain with the  
814 contours (every 0.5 m) of the slip model shown in Fig. 9a, together with aftershock locations  
815 from a local network (small yellow circles, Pacheco et al. 1997), as well as corrected aftershock  
816 locations (see text) from global networks (larger circles). Timing of aftershocks is shown with  
817 progression from white (first day after earthquake) to black (five days after earthquake and later)  
818 circles.

819

820 **Figure 10.** Predicted tsunami wave height 9 minutes after earthquake for three different models:  
821 a) Seismic (w0.001), b) Joint Seismic and GPS (w0.1), c) GPS (w1.0) d) Corresponding  
822 estimated waveforms compared to the CTD mooring/pressure sensor offshore Barra de Navidad  
823 (amplitude scaled by 0.5). e) Calculated tsunami wave heights along the coast compared to the  
824 post-tsunami survey observations.

825

826 **Figure 11.** Slip on fault for the best fit seismic only model (Fig. 3f) and for the joint model with  
827 weight 0.1 (Fig. 6e). Slip amplitude is shown with colors, direction with white arrows and  
828 timing of rupture at each point with black rupture contours. The contours are very dense in the  
829 large slip or red patch, suggestive of a slower rupture velocity.  
830

**Figure 1.**

MESO AMERICAN TRENCH

1932a

Puerto Vallarta

Careyitos

1995

JALISCO

La Manzanilla

Santiago Bay

Manzanillo

COLIMA

Guadalajara

MICHOACAN

RIVERA PLATE

PACIFIC PLATE

Barra de Navidad

1932b

2003

1973

1985

COCOS PLATE

100 km



**Figure 2.**

## TSUNAMI WAVE HEIGHTS AND STATIC OFFSETS

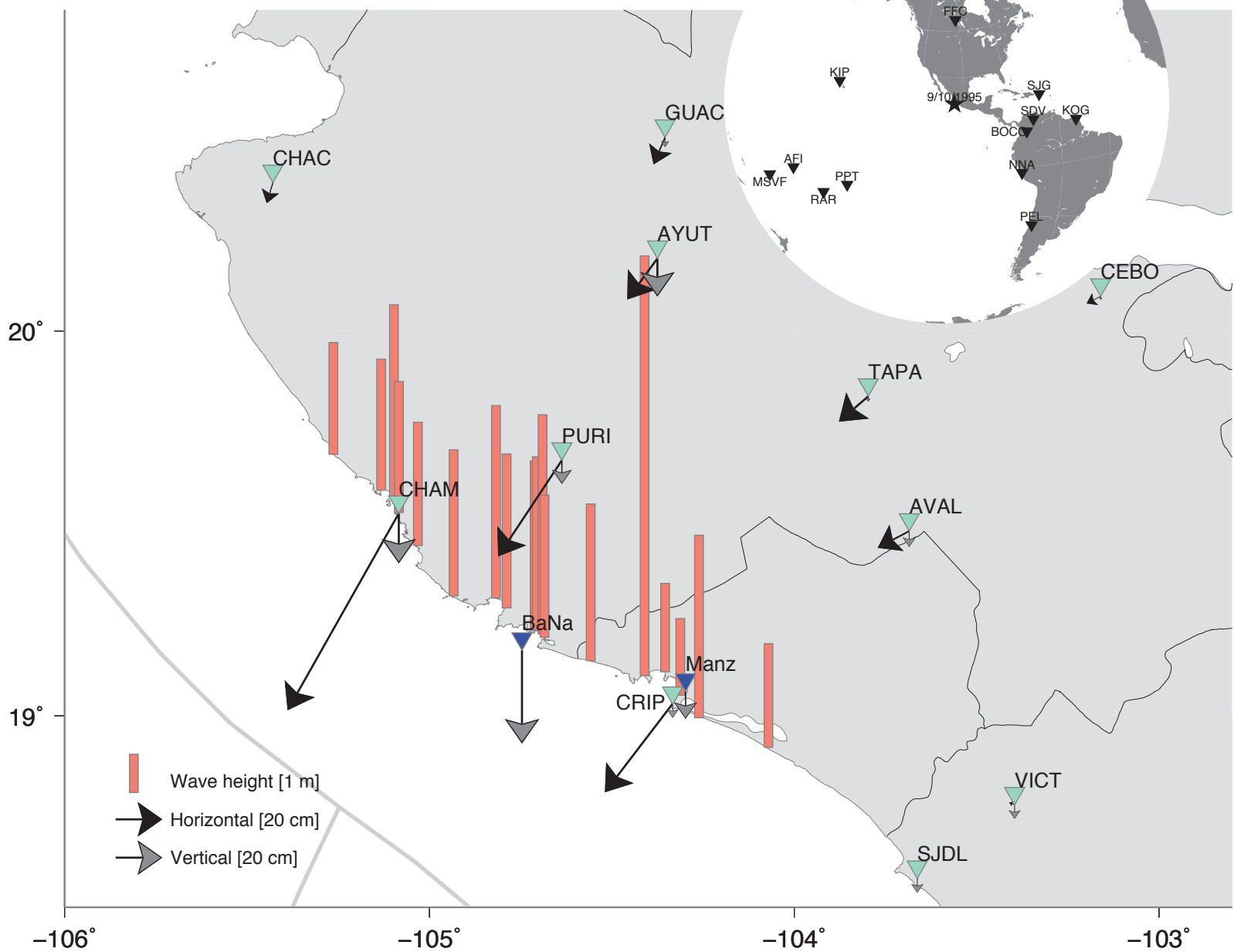


**Figure 3.**

# SEISMIC ONLY INVERSION

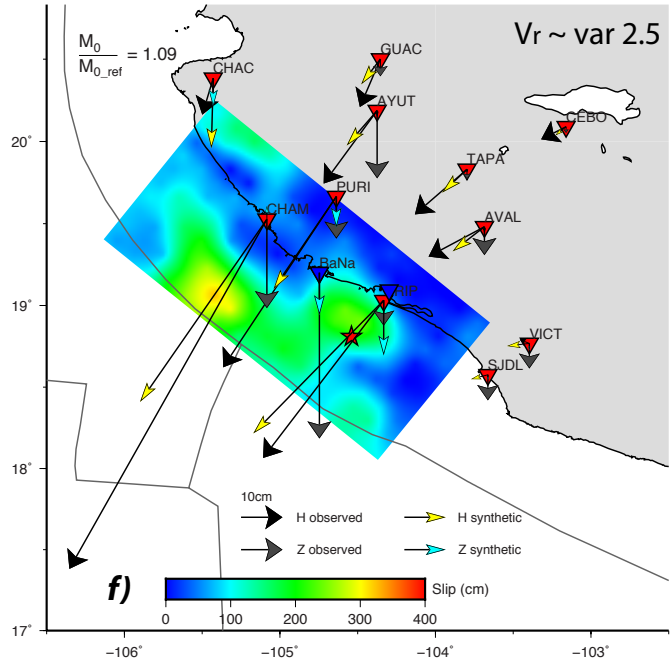
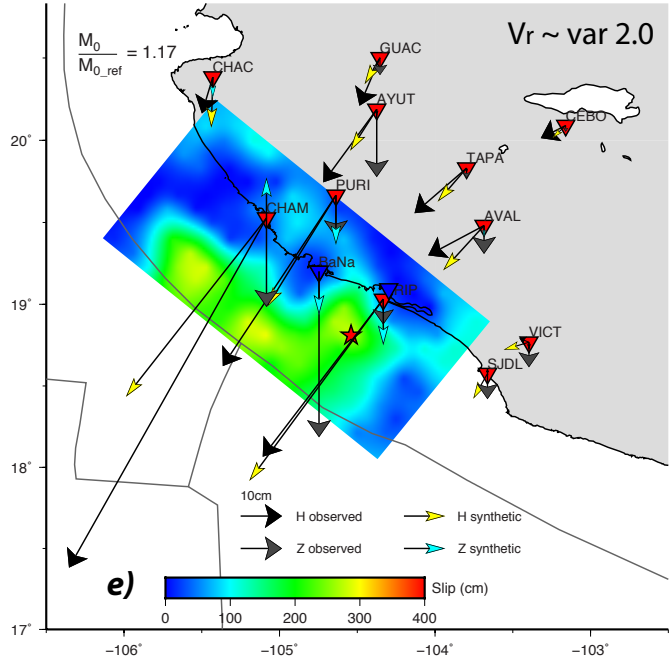
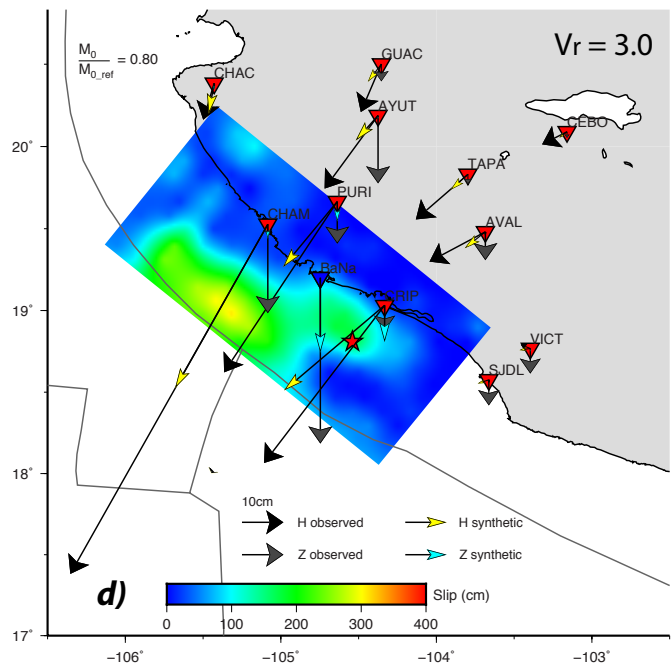
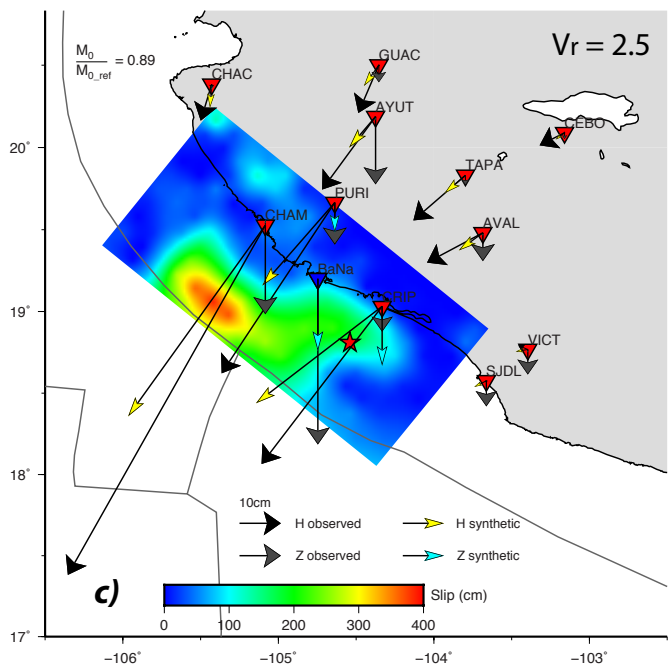
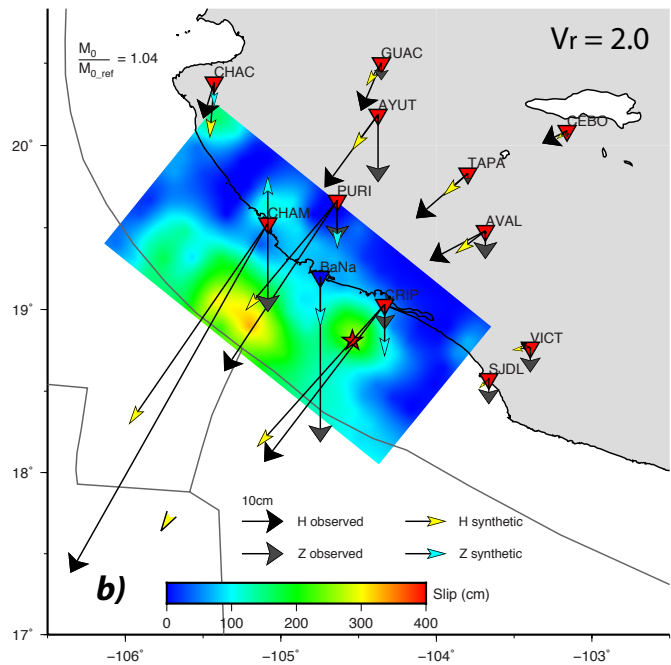
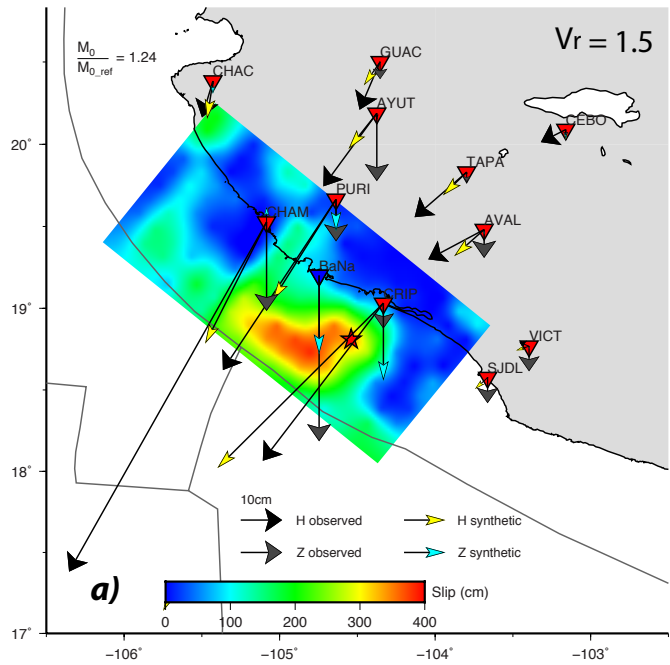


**Figure 4.**

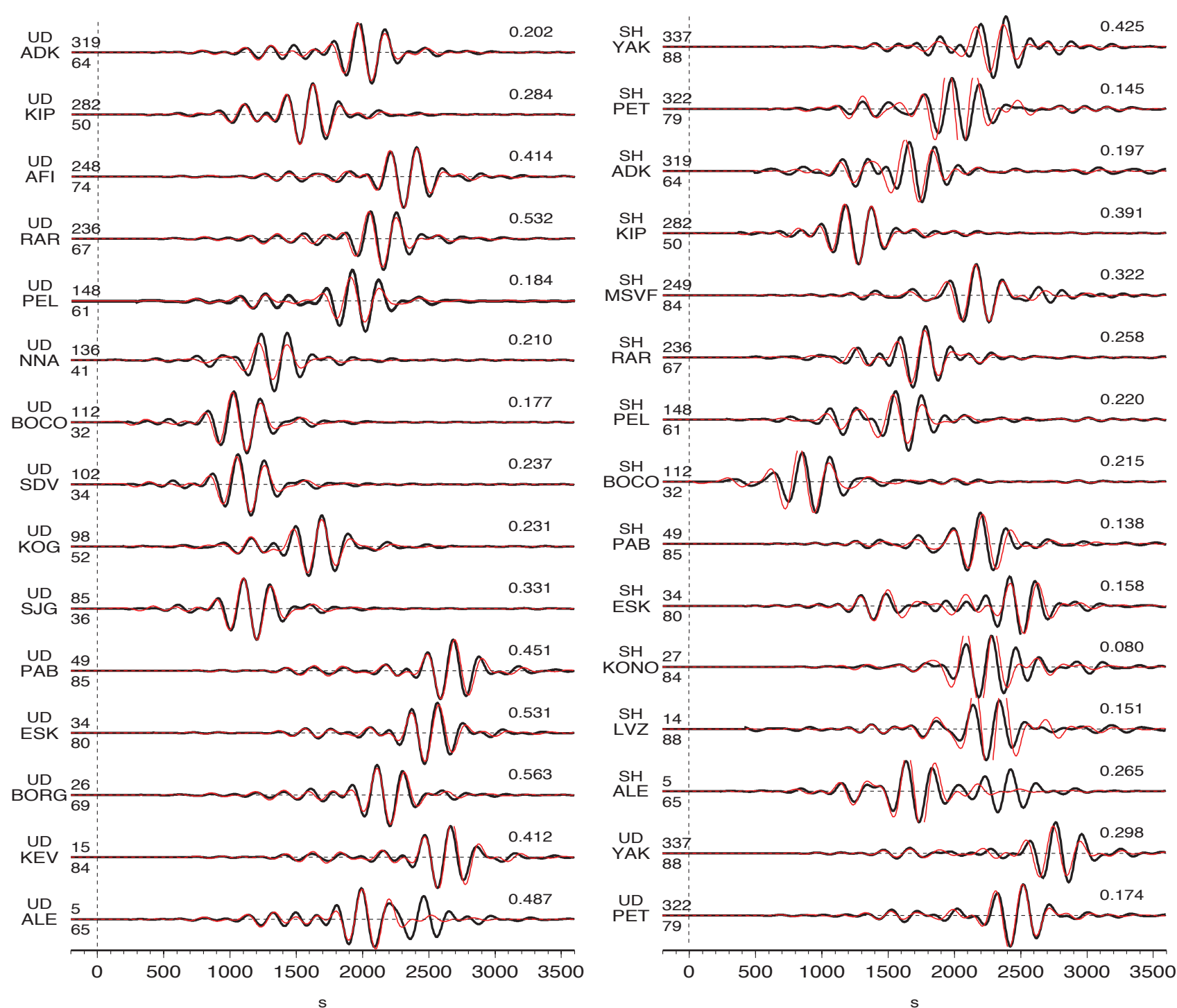
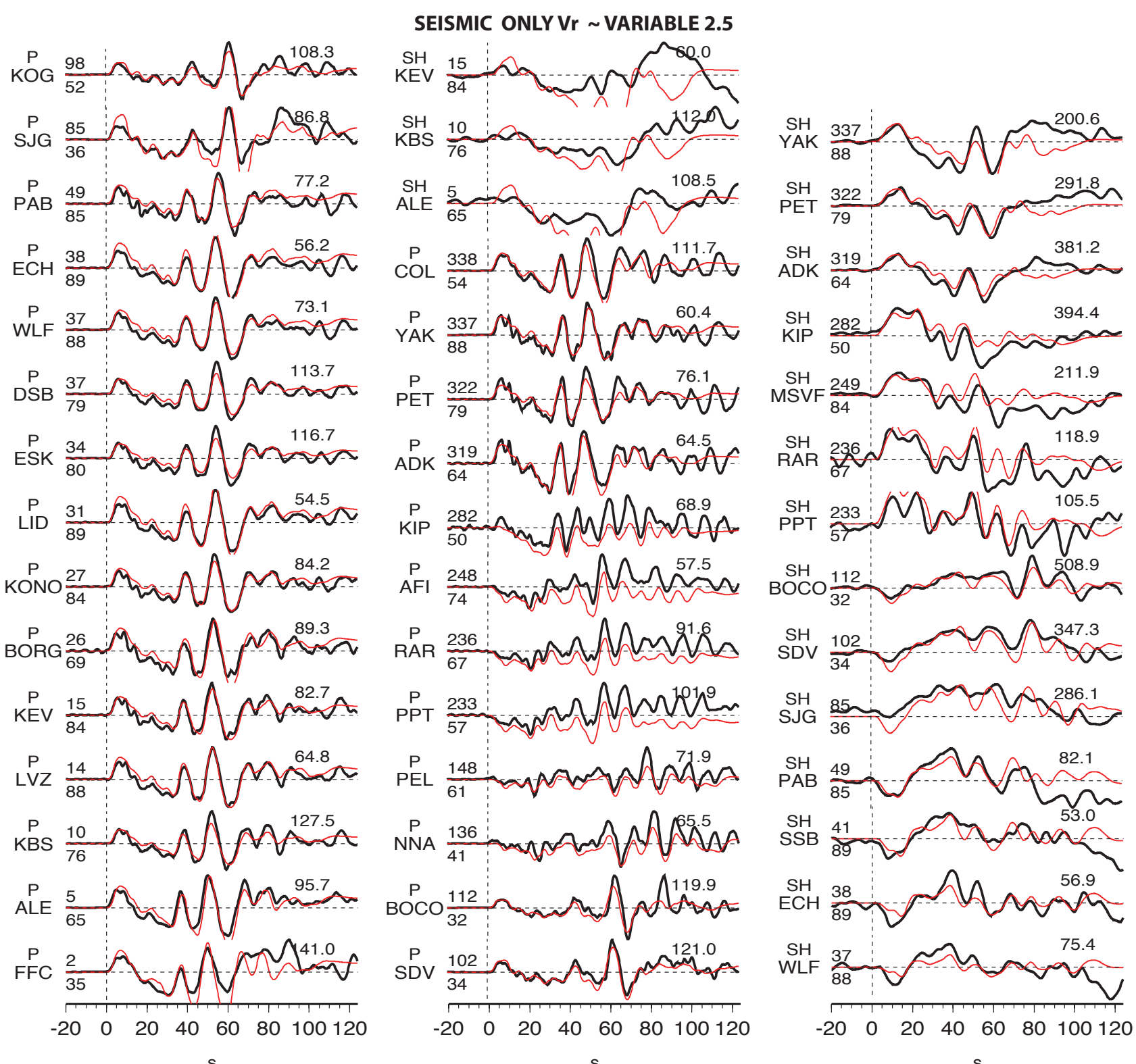


**Figure 5.**

# STATIC INVERSION

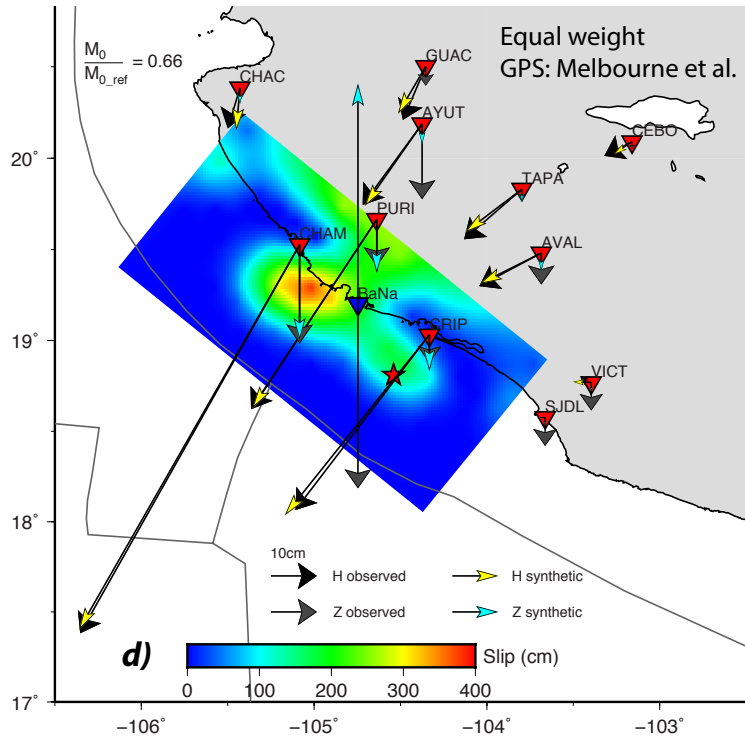
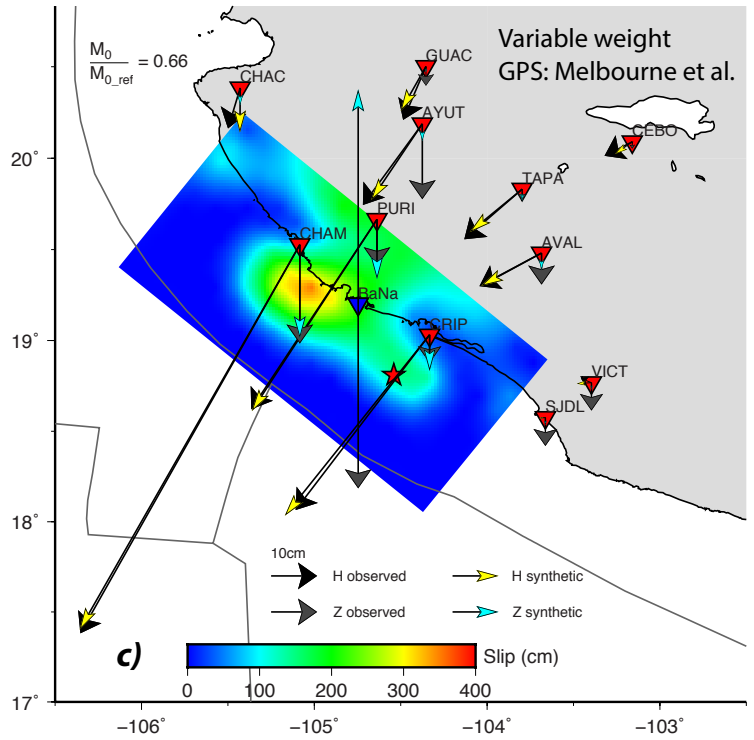
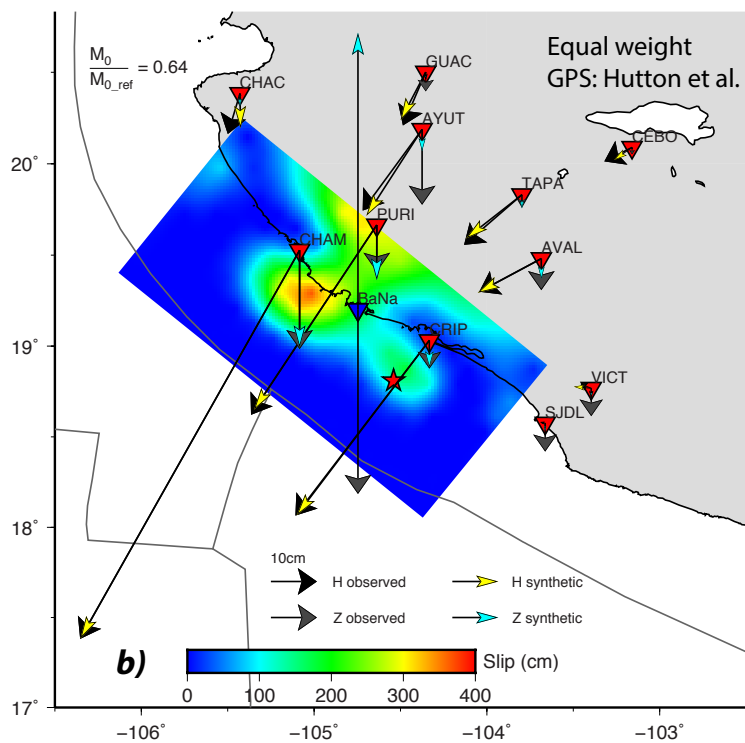
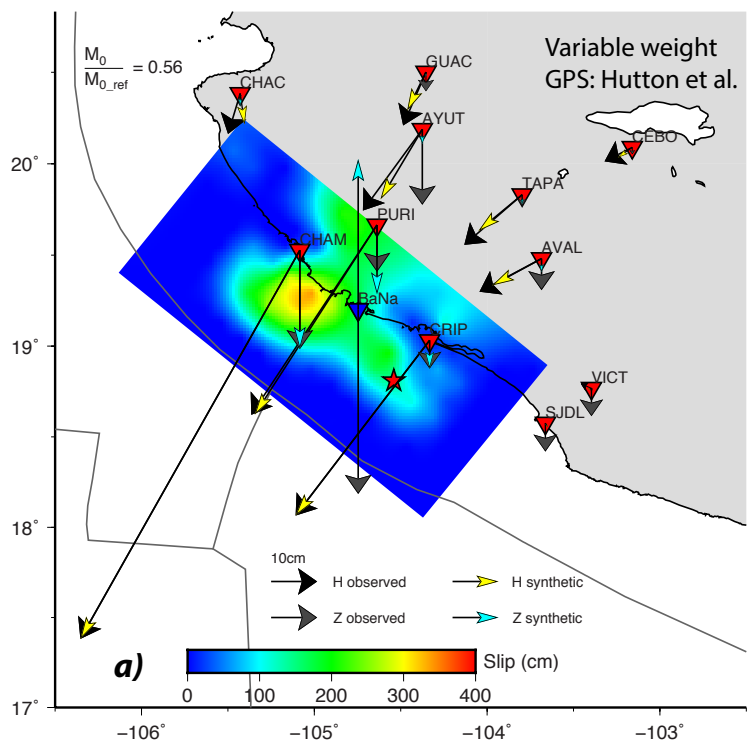


**Figure 6.**

# JOINT INVERSION

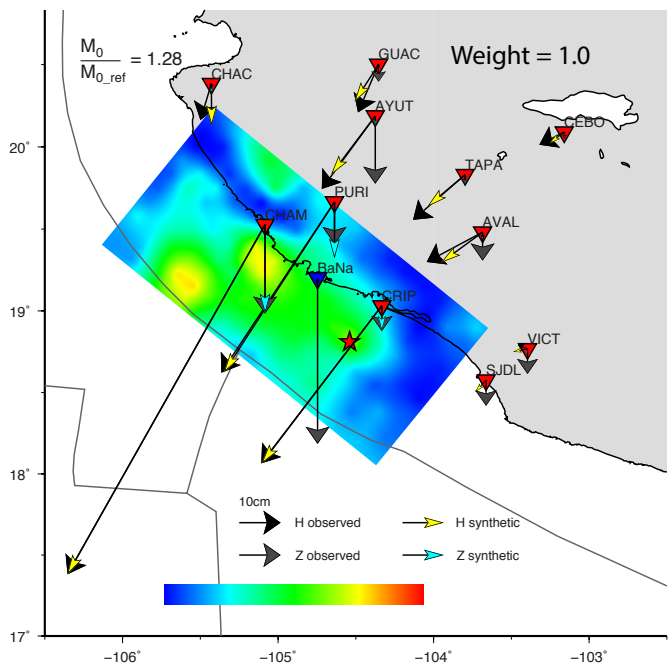
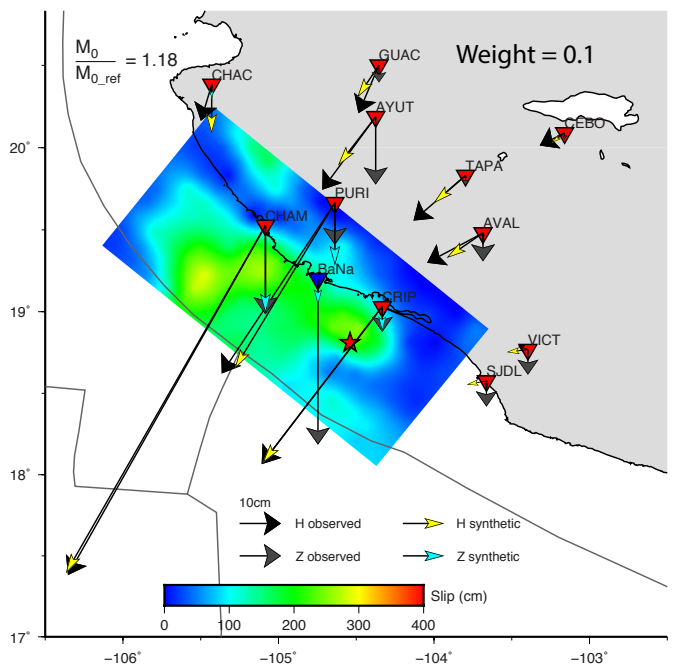
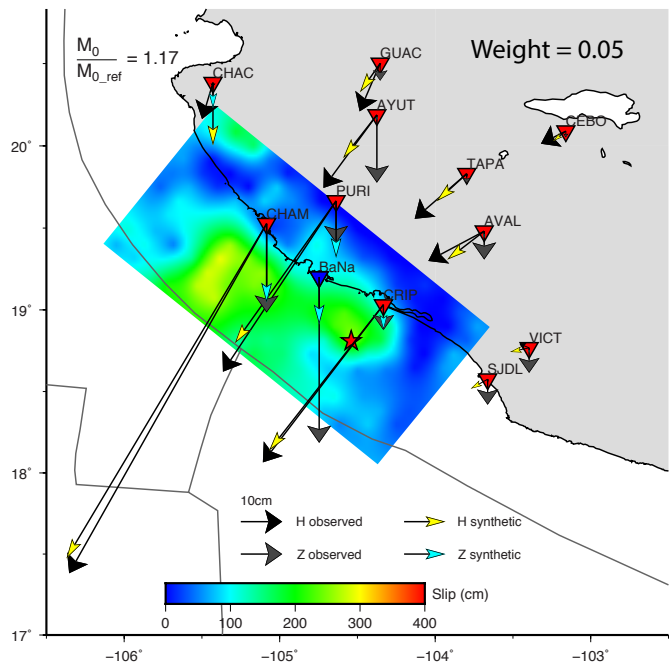
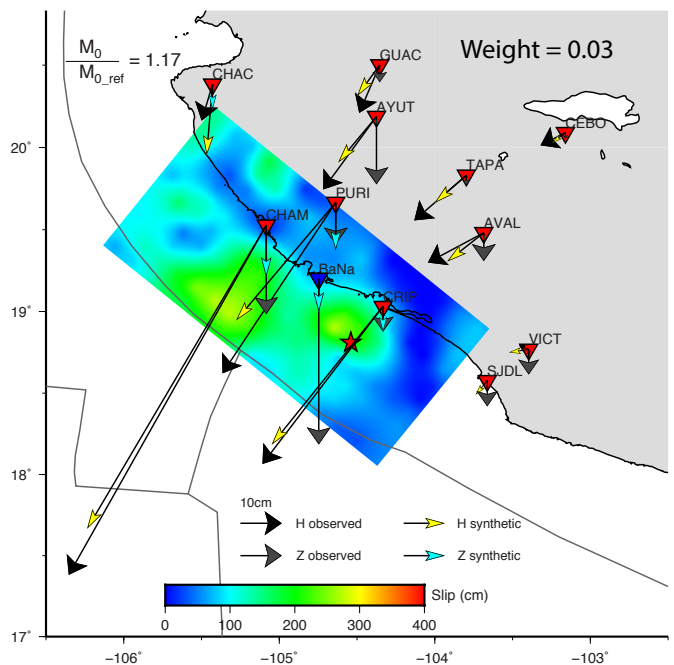
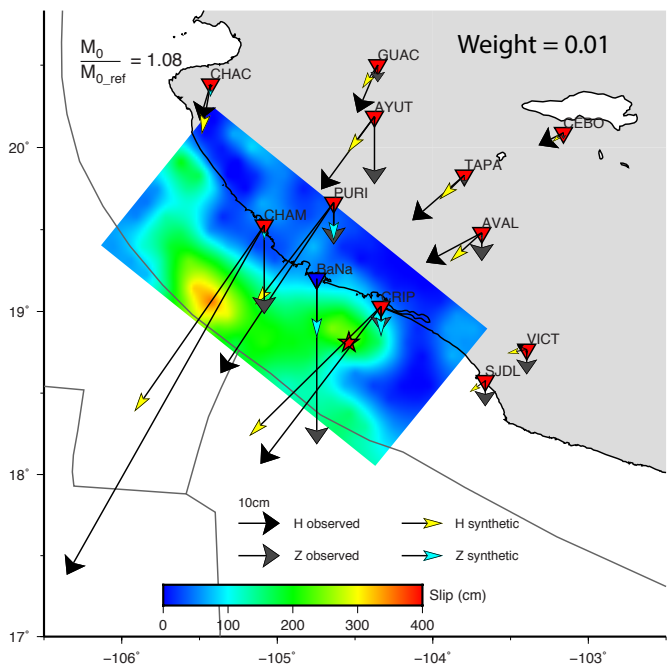
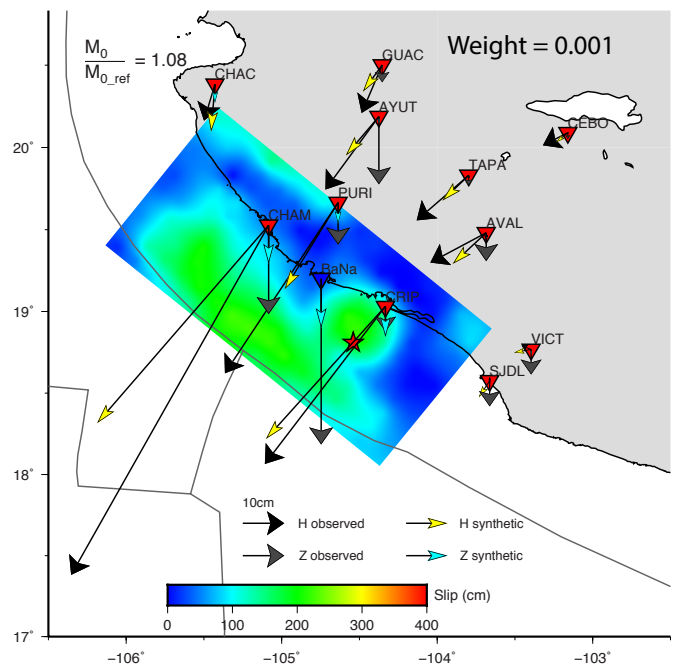


**Figure 7.**

# JOINT SEISMIC AND GPS . WEIGHT = 0.1

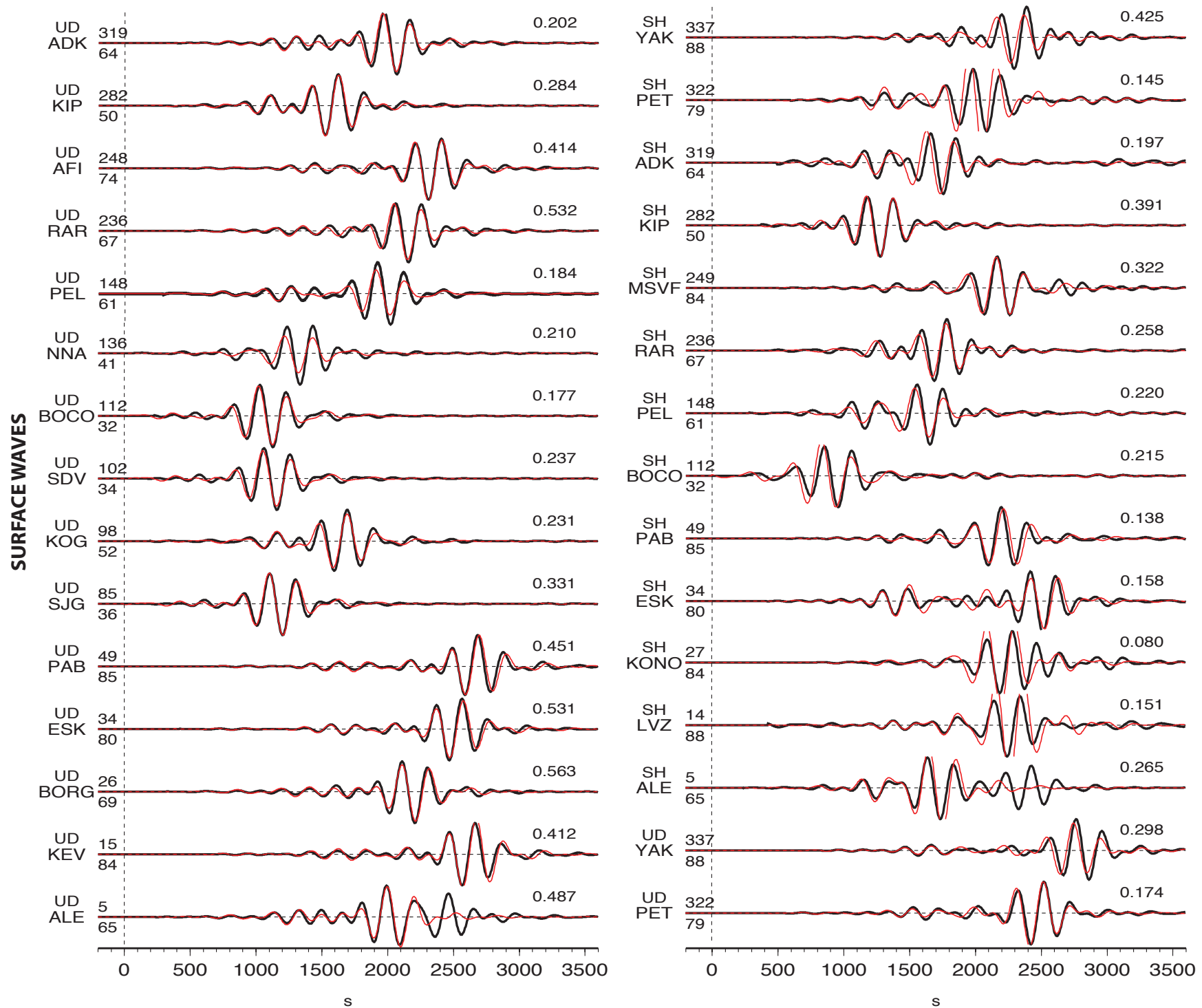
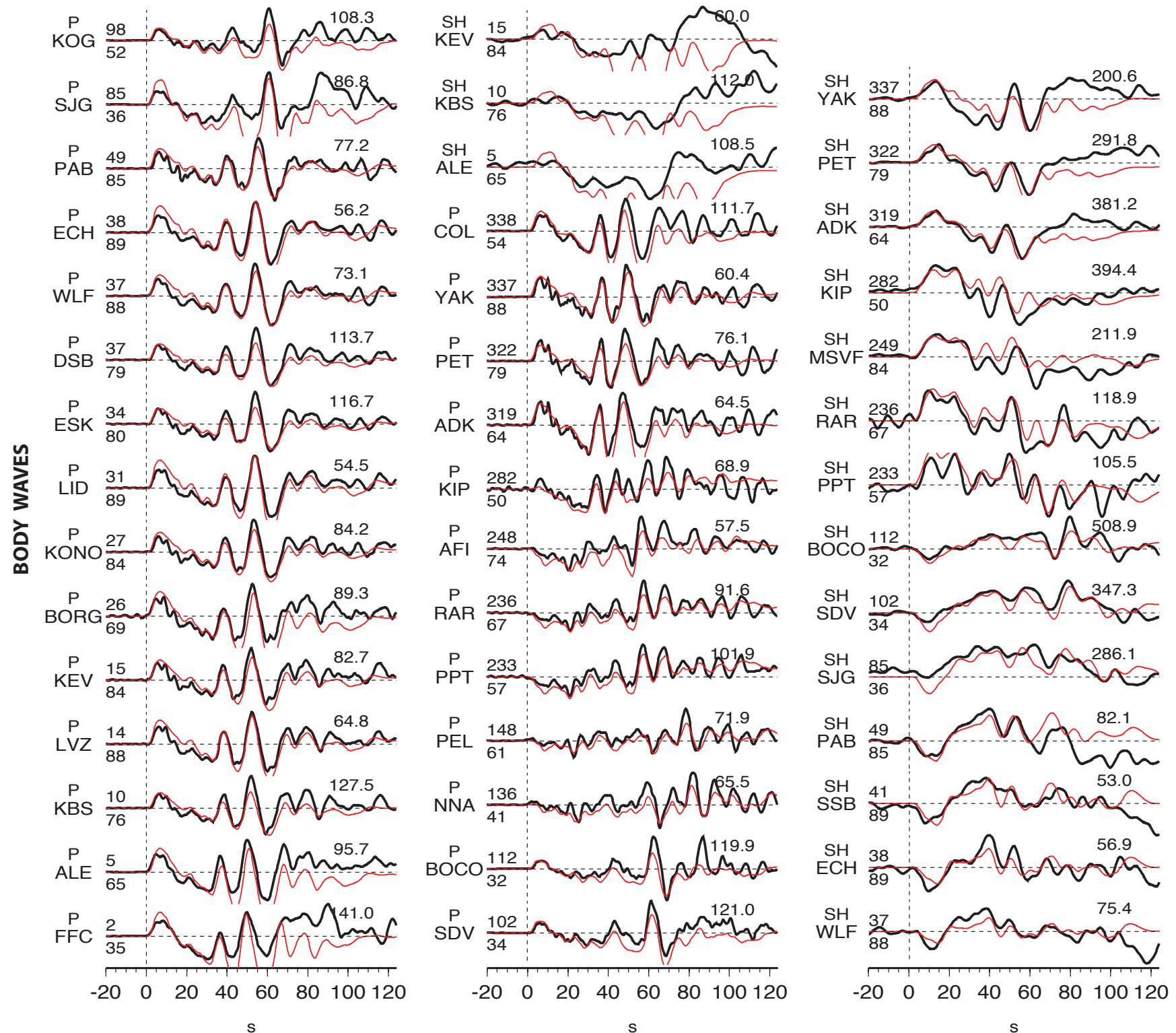
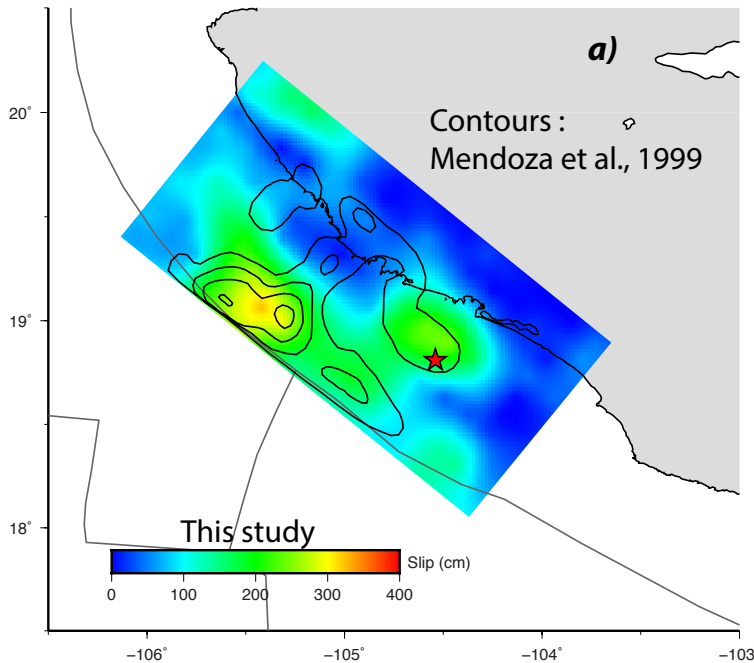


**Figure 8.**

## SEISMIC SLIP MODEL

*a)*

Contours :  
Mendoza et al., 1999



## STATIC SLIP MODEL

*b)*

Contours :  
Hutton et al., 2001

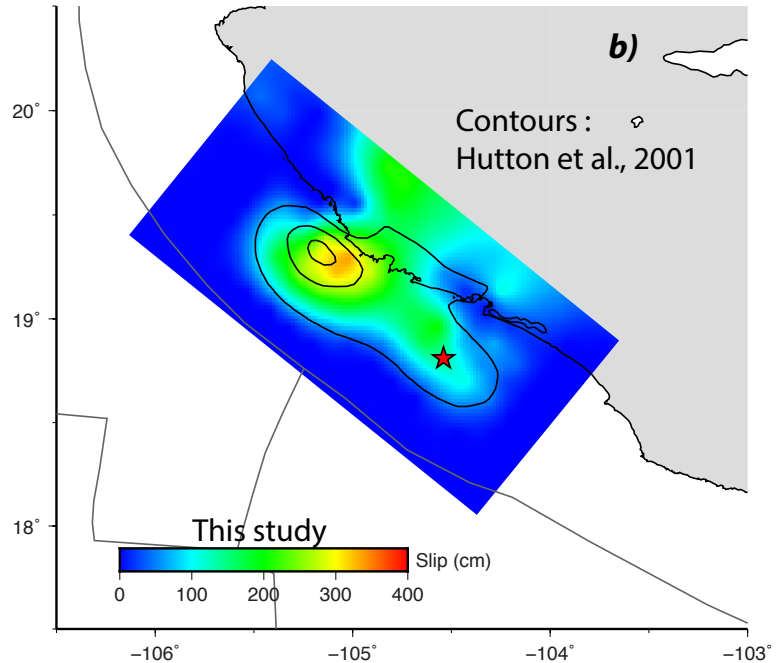
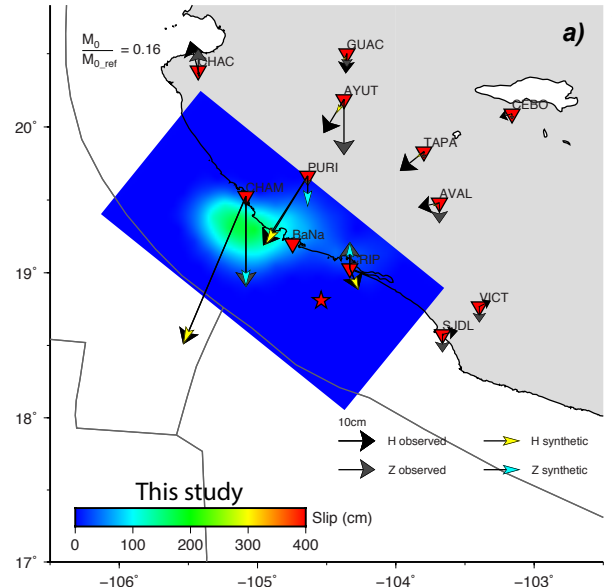


**Figure 9.**

## ASEISMIC SLIP



## COSEISMIC VS AFTERSLIP

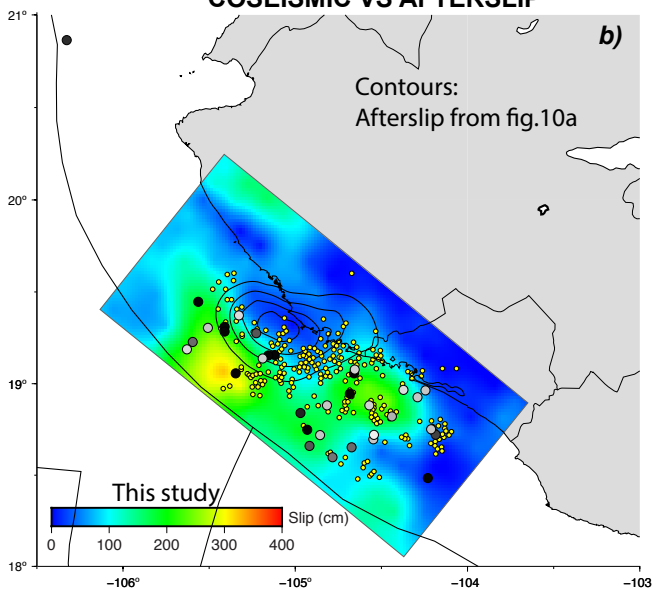
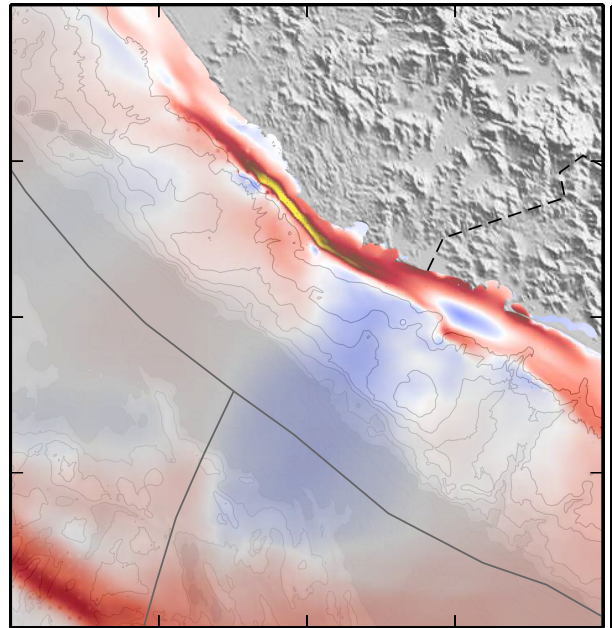


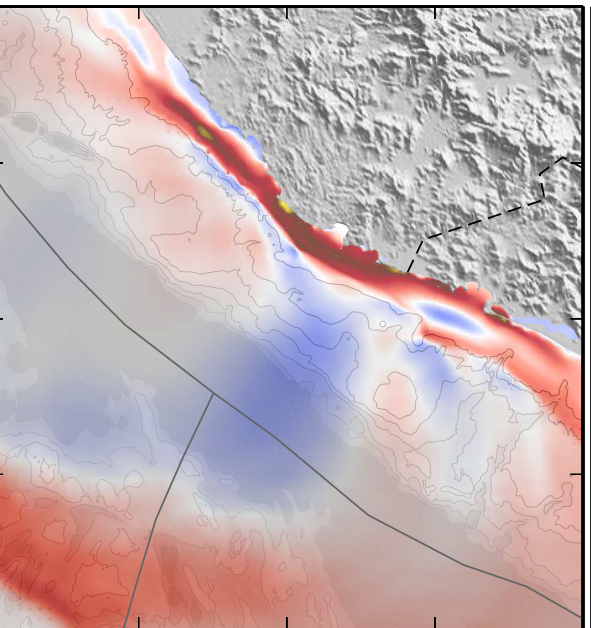
**Figure 10.**

# TSUNAMI WAVE HEIGHTS

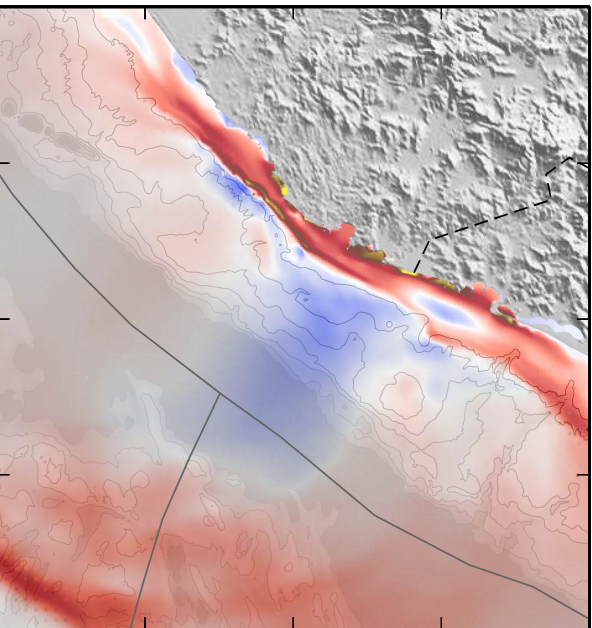
a



b

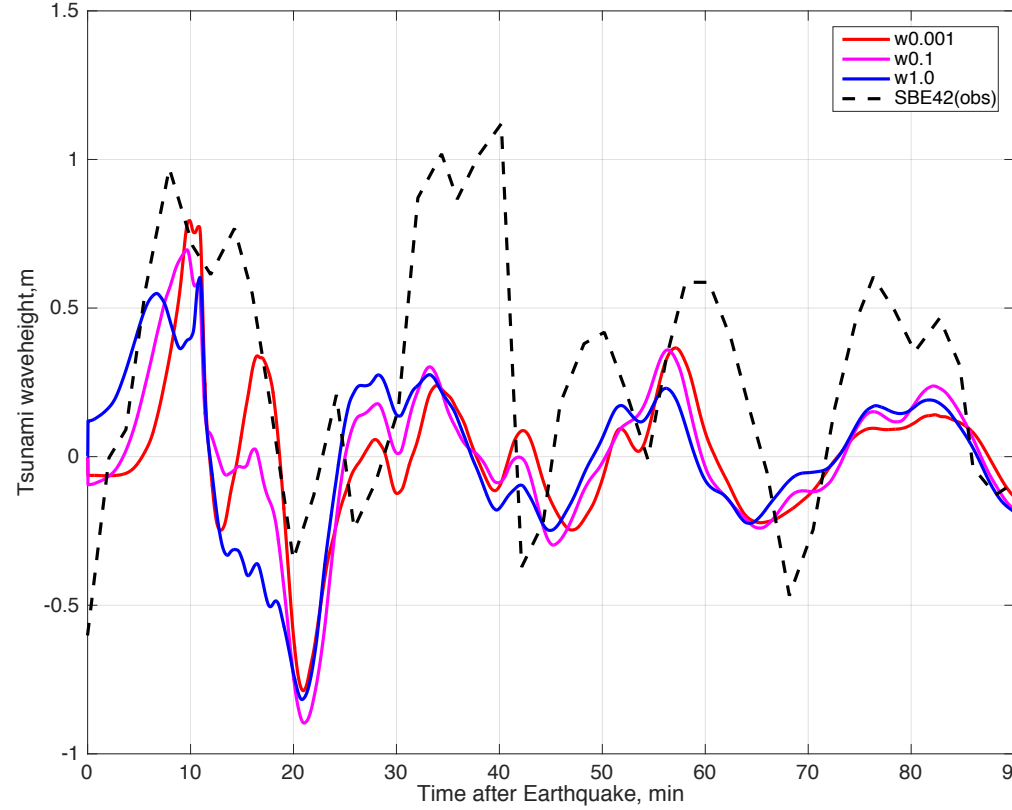


c



# TSUNAMI WAVE HEIGHT, PRESSURE SENSOR

d



# WAVE HEIGHTS ALONG COAST

e

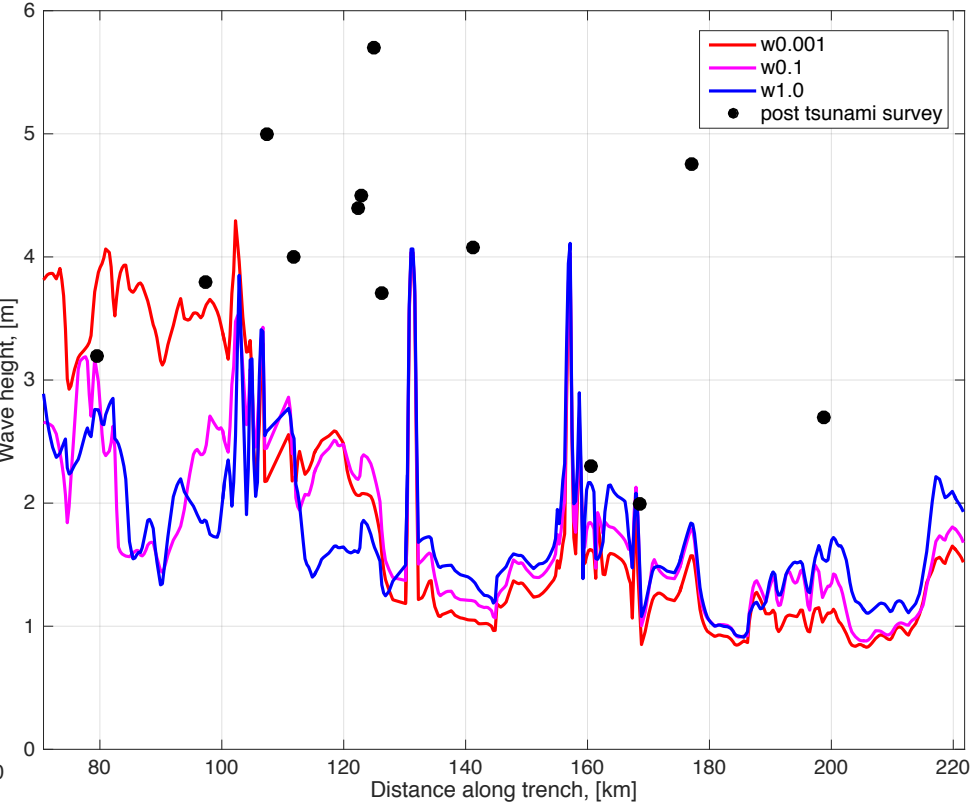
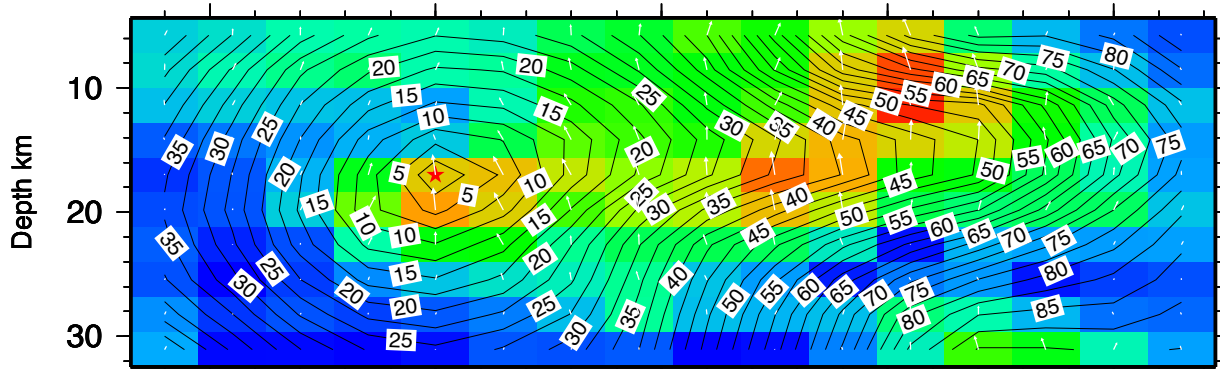


**Figure 11.**

### SEISMIC ONLY Vr= var 2.5



### JOINT

